https://doi.org/10.5194/essd-2025-757
Preprint. Discussion started: 21 January 2026

Open Access Earth System Science Data Discussions

Daily melt pond and net ice surface fractions in the Arctic Ocean from MODIS visible imagery: 2000 - 2024

Remon Sadikni[1], Stefan Kern[1]

[1]Integrated Climate Data Center (ICDC), University of Hamburg, Hamburg, 20144, Germany

Correspondence to: Stefan Kern (stefan.kern@uni-hamburg.de)

Abstract. We report on a novel data set of the melt-pond fraction on Arctic sea ice. Melt ponds on Arctic sea ice are an important phenomenon of the summer-melt process. They reduce the surface albedo of sea ice substantially, by that influence the net shortwave radiation balance, and with that the amount of solar radiation energy that is received by the sea ice-ocean system in the Arctic during summer. This has also implications for under-ice biogeochemical processes and ice mechanics. Melt ponds have been observed by a number of satellite sensors, mostly in the optical and near-infrared wavelength range. Here we present an updated version of a spectral un-mixing approach published earlier that led to a data set of melt-pond fraction on Arctic sea ice with 8-daily sampling for months May through August from 2000 through 2011. The approach is based on reflectance measurements of channels 1, 3 and 4 of the Moderate Resolution Imaging Spectroradiometer MODIS on board the Earth Observation Satellite (EOS) Terra satellite. We modified the approach and derived the daily melt-pond fraction on Arctic sea ice at 500 m and at 12.5 km grid resolution for months June through August from 2000 through 2024 from MODIS v6.1 observations. In addition, we provide the net ice surface fraction – aka the fraction of sea ice without melt ponds – and the fraction of open water between the ice floes. Our MODIS melt-pond fraction agrees within -3 % to +4 % with independent estimates of the melt-pond fraction from very-high resolution optical satellite imagery and from Operation Ice Bridge Digital Camera System imagery. The MODIS open-water fraction we find to be too small by 2 % to 6 %; the net ice-surface fraction tends to be too large by 2 % to 9 %. The 12.5 km gridded product shows a slightly worse (by 1 %) agreement. While our 12.5 km gridded MODIS product under-estimates the melt-pond fraction from very-high resolution optical satellite imagery by about 2 % in the mean (median: 3 %), the Medium Resolution Imaging Spectrometer (MERIS) product over-estimates these independent estimates by about 8 % (median: 9 %). Our MODIS melt-pond fraction data set is available from Sadikni and Kern (2025): https://doi.org/10.25592/uhhfdm.18069.

1 Introduction

In this contribution, we are presenting a novel 25-years long time series of the melt-pond fraction on Arctic sea ice for the months June to August. Melt ponds are puddles of melt water that form on Arctic sea ice during summer melt. They usually form first where melt water from melting snow accumulates in depressions of the sea ice topography. After snow melt they continue to spread and deepen as consequence of sea ice melt. The typical size of a melt pond is about 10 m² (e.g. Perovich

https://doi.org/10.5194/essd-2025-757
Preprint. Discussion started: 21 January 2026

et al., 2002a) albeit substantially larger but also smaller melt ponds coexist. The size distribution (and depth) of melt ponds on Arctic sea ice depends on the surface topography and the sea ice type (e.g. Petrich et al., 2012; Perovich and Polashenski, 2012). Typical melt-pond fractions, i.e. the fraction of the sea ice covered with melt water in form of a melt pond, range between about 10 % for multiyear ice and around 30 % for first-year ice (Polashenski et al., 2012). Land-fast sea ice or other sea ice with a particularly level surface can be covered with melt ponds by 50 % or even more (e.g. Barber and Yackel, 2000; Landy et al., 2014). Both the size and the distribution of melt ponds undergo a seasonal cycle and are determined by the geographical latitude and the amount of solar radiation received by the surface. For more information about melt ponds on Arctic sea ice we refer to Polashenski et al. (2012) and Webster et al. (2015).

Melt ponds are an important element of the Arctic sea ice's seasonal cycle. They exhibit a considerable lower surface albedo than the still snow-covered or bare sea ice next to them. Melt ponds therefore allow much more solar radiation to enter the snow-sea ice-ocean system and hence determine the pan-Arctic albedo of sea ice during summer. The timing of melt-pond formation plays an important role for both the further development of the melt-pond coverage during the summer melt season and the development of the sea ice cover itself (Perovich and Polashenski, 2012; Perovich, 2018). The larger the melt-pond cover fraction is and the earlier a considerable coverage with melt ponds develops the lower gets to overall albedo of the Arctic sea ice cover and the more solar radiation is received, enhancing melt and further increasing melt-pond cover fraction and melt-pond depth, contributing to weakening the sea ice cover mechanically. Melt ponds can also be considered as windows to the underlying ocean as they are sites of a snow free and thinner sea ice cover, enhancing the sub-ice light levels and thereby contributing to plankton and algal growth (e.g. Kramer and Kiko, 2010; Palmer et al., 2014; Lu et al., 2016).

Direct observations of melt ponds and/or the melt-pond fraction on sea ice are sparse and limited to ship-based expeditions into the Arctic Ocean. While such expeditions, e.g. SHEBA or MOSAiC (see also Aparício et al. (2025)), have provided the foundation of our understanding of the formation mechanism of melt ponds, including their seasonal cycle (e.g. Fetterer and Untersteiner, 1998; Perovich et al., 2002a,b; Sankelo et al., 2010), they are an inadequate tool to observe the Arctic melt-pond fraction in its entirety. Here, like for many other sea-ice quantities, satellite observations have proven to be a reliable possibility to detect and monitor melt ponds on sea ice. Satellite observations in the visible / near infrared frequency range have been used, e.g., from Landsat-7 Enhanced Thematic Mapper (ETM) (Markus et al., 2003), from the Medium Resolution Imaging Spectrometer (MERIS) (Istomina et al., 2015a,b; Zege et al., 2015; Istomina et al., 2025), from MODIS (Tschudi et al., 2008; Rösel et al., 2012; Lee et al., 2020), and from Sentinel-2 Multispectral Instrument (MSI) (Wang et al., 2020; Niehaus et al., 2023) and Sentinel-3 Ocean and Land Colour Instrument (OLCI) (Niehaus et al., 2024; Istomina et al., 2025). All these approaches require daylight (which only becomes a limitation in late summer, e.g. September) and cloud-free conditions. The latter can be a serious limitation as can be seen later in this contribution. While one could overcome these limitations by using satellite sensors operating in the microwave frequency range, attempts to derive the melt-pond fraction from such observations remain problematic. These are limited to special cases and/or the delineation of the seasonal cycle of melt events rather than obtaining the melt-pond fraction (e.g. Yackel and Barber, 2000; Scharien et al., 2012; Mäkynen et al.,

https://doi.org/10.5194/essd-2025-757
Preprint. Discussion started: 21 January 2026

2014; Tanaka et al., 2016; Fors et al., 2017; Howell et al., 2020). Recently satellite laser altimetry has been used to detect melt ponds on Arctic sea ice (e.g. Tilling et al., 2020). Aparício et al. (2025) provide an overview of observational data sets related to melt ponds on Arctic sea ice.

The data set we are presenting in this contribution is based on the approach of Rösel et al. (2012), which is briefly described in the Methods section, and which led to a first version of the data set (Rösel et al., 2013), being bias-corrected later (Rösel et al., 2015). While the approach of Rösel et al. (2012) used 8-daily Terra MODIS reflectance observations (MODIS processing version 4) and hence provided a melt-pond fraction data set with 8-daily resolution, our new product comes with daily temporal resolution as it is based on daily MODIS reflectance observations. The Rösel et al. (2013; 2015) data set covers years from 2000 through 2011; our data set covers years from 2000 through 2024. Similar to the Rösel et al. (2013, 2015) melt-pond fraction data set, we are providing our data set on a 12.5 km grid resolution polar-stereographic grid and include, in addition to the grid-cell fraction of melt ponds, also the grid-cell fractions of sea ice free of melt ponds and of open water between the ice floes. We provide the data set at 500 m grid resolution as well. In the following, we describe the modification of the approach by Rösel et al. (2012), provide estimates of area-mean melt-pond fraction data, and present and discuss results of our evaluation activities.

2 Data

In this section, we detail the input data used to generate our melt-pond fraction data set. We also briefly describe the data sets used for product evaluation and inter-comparison.

2.1 Input Data

Our daily melt-pond fraction data set is available here (Sadikni and Kern, 2025): https://doi.org/10.25592/uhhfdm.18069. It is derived from observations of the MODerate resolution Imaging Spectroradiometer MODIS aboard the Earth Observation Satellite (EOS) Terra. We use the MODIS collection 6.1 product MOD09A1 of the surface spectral reflectance. We downloaded data of all MODIS sinusoidal grid tiles north of 60°N – aka v2 h9-h26, v1 h12-h23, and v0 h15-h20 from https://lpdaac.usgs.gov/products/mod09gav061/ (last access: 2024-12-06). Further details of the pre-processing of this data are given in section 3.1.

2.2 Evaluation and Inter-comparison Data

Here we introduce three data sets used for the evaluation of the melt-pond fraction data set at 500 m grid resolution and two independent gridded melt-pond fraction data sets based on satellite observations of the MERIS (subsection 2.2.4) and OLCI (subsection 2.2.5) sensors for the inter-comparison and evaluation of our data set at 12.5 km grid resolution.

https://doi.org/10.5194/essd-2025-757
Preprint. Discussion started: 21 January 2026

2.2.1 Surface fractions from high-resolution visible band satellite imagery

We used two different data sets of melt-pond fraction on sea ice derived from high-resolution (~ 1 m) visible band satellite imagery (see Fig. 3 for their locations). One is the Fetterer et al. data set (Fetterer et al., 2008; http://nsidc.org/data/G02159/versions/1, last access: 2023-09-05); the other one is the Webster et al. data set (Webster et al., 2015; http://psc.apl.uw.edu/melt-pond-data/, last access: 2023-09-05).

For the Fetterer et al. data set, visible band high-resolution satellite imagery were acquired over the Arctic Ocean's multiyear ice cover in the summers of 1999, 2000, and 2001, spaced irregularly in time. Using supervised maximum likelihood classification the clear-sky parts of the images were classified into either two (water and ice) or three (pond, open water, and ice) surface classes. The original data set consists of tables of pond coverage and size statistics for 500 m square cells within the between 1 km and 10 km square satellite images from which the surface type maps called Image Derived Products (IDPs) and pond statistics were derived. We used the summary of the IDPs where the melt-pond fraction of the entire scene is provided along with its sea-ice concentration, both in percent, the scene dimension and geolocation information. The melt-pond fraction is given relative to the sea-ice cover fraction. Since the first summer covered by MODIS data is from the year 2000 we used Fetterer et al. data only in the years 2000 and 2001. We excluded two images from September and two images from August 31 in the year 2000. Cloud coverage in the MODIS images reduced the number of useful images to a total of 25 scenes being useful for our evaluation.

The Webster et al. data set (Webster et al., 2015) is based on de-classified U.S. National Technical Means and U.S. National Imagery Systems high-resolution visible panchromatic satellite imagery acquired at irregularly times within years from 2000 through 2014. Image scenes are between 5 km and 25 km square image size and have 1 m spatial resolution. Cloud cover and shadow-screened scenes were analysed using a supervised multistep classification using physically based thresholds and considering neighbouring pixels' intensities. Further details of the methodology used are given in Webster et al. (2015). We are using a tabulated version of this data set, containing a value of the entire scene melt-pond fraction along with its sea-ice concentration, both in percent, the scene dimension and geolocation information – similar to the Fetterer et al. data set. Also here, the melt-pond fraction is given relative to the sea-ice cover fraction. The data set contains 75 scenes, all but one falling into months May through August, of which we actually used 65 scenes – again due to cloud cover identified in the MODIS images.

2.2.2 Surface fractions from high-resolution optical airborne imagery

One element of the airborne NASA Operation IceBridge (OIB) campaigns is the Digital Mapping System (DMS). This system takes optical images with a Canon EOS 5D Mark II digital camera, which at the nominal flight altitude of 1500 feet provides a spatial resolution of 0.1 m for an image size of approximately 600 m x 400 m (Dominguez et al., 2010, updated 2017). Based on these images two data sets of the melt-pond fraction on sea ice were derived (Wright and Polashenski, 2018; Wright et al., 2020; Buckley et al., 2020). We used the Buckley et al. data set for both a qualitative fine-tuning of the values

https://doi.org/10.5194/essd-2025-757
Preprint. Discussion started: 21 January 2026

of the spectral reflectances chosen (see Table 1) and for the evaluation, while we used the Wright et al. data set as an independent means for the evaluation of our MODIS melt-pond fraction data set at 500 m grid resolution.

The Wright et al. data set (Wright and Polashenski, 2018; Wright et al., 2020) utilized Level 0 (raw) digital imagery for a classification of the reflectivity values into surface types using the Open Source Sea-ice Processing (OSSP) algorithm. After some pre-processing the OSSP algorithm combines segmentation, filtering, watershed transformation and random forest classification to generate maps containing the four surface types: open water, melt pond, dark ice (which includes submerged ice) and snow+ice (i.e. brighter ice surfaces). We used a subset of this data set covering eight flights in total during July 2016 and July 2017 (Polashenski et al., 2020, https://doi.org/10.5067/1LI57H56EB7G, last access: 2021-10-06). We downloaded the data as .csv files containing a quality score and the portion of the image covered by surface classes white ice, grey ice, melt ponds, open water, and shadow. We only used data from images with a quality score above 0.3 (see Wright et al., 2020) and sub-summed white ice and grey ice into ice surface fraction (ISF). We read coordinates from the associated .xml files downloaded from the same source. The melt-pond fraction is given relative to the size of the image and hence are directly comparable to our MODIS melt-pond fraction data set.

The Buckley et al. data set (Buckley et al., 2020) utilized Level 1B RGB digital imagery from OIB DMS. The RGB channel information was exploited in an automated pixel-based classification algorithm utilizing histogram-based threshold selection to iteratively first define sea ice pixels, then identify open water pixels and subsequently distinguish open water between ice floes and melt ponds on the sea ice. While the algorithm also classifies different regimes of melt pond colour, we only use the melt-pond fraction. Data are provided for the same dates as the Wright et al. data set (eight days in July 2016 and 2017) as .txt files from ftp://ftp.star.nesdis.noaa.gov/pub/socd/lsa/SeaIceProducts/Airborne/IceBridge/SummerMelt/ (last access: 2021-09-24) and contain the melt-pond fraction, the sea-ice concentration, the fractions of dark, medium and light melt ponds, and coordinate information. The melt-pond fraction is given relative to the sea-ice cover fraction, necessitating conversion of this fraction (and the ice surface fraction) into an estimate relative to the image size.

2.2.3 University of Bremen MERIS melt-pond fraction

MERIS was flown on the Envisat satellite of the European Space Agency (ESA) providing observations of the Earth in the visible / near-infrared part of the electromagnetic spectrum between 412.5 nm and 900 nm. Of the 15 spectral channels provided, observations from eight channels were used by Zege et al. (2015) to derive maps of the surface spectral albedo and a per grid cell melt-pond fraction. The algorithm developed by Zege et al. (2015) is a multistep process, beginning with a cloud-screening, continuing with defining ice covered grid cells by means of using reflectance values of MERIS channels 2, 3 and 4, and with a core-part of the algorithm where a Newton-Raphson iteration method is applied to separate white ice from melt ponds. The resulting melt-pond fraction data set is distributed on a 12.5 km polar-stereographic grid with tangential plane at 70°N latitude with daily temporal resolution for months May through September for the period from 2002 through 2011. The algorithm itself and the melt-pond fraction has been validated (Zege et al., 2015; Istomina et al., 2015a,b, 2023) and further enhanced by applying an improved cloud masking scheme (Istomina et al., 2020a). We use data of months

https://doi.org/10.5194/essd-2025-757
Preprint. Discussion started: 21 January 2026

May through August of this latest improved version of the MERIS melt-pond fraction data set: MPD1.7 (Istomina et al., 2023, https://data.seaice.uni-bremen.de/meris/mecosi/, last access: 2023-10-26).

2.2.4 University of Bremen OLCI melt-pond fraction

OLCI has been flying on the ESA Sentinel-3 satellites since February 2016 (S3A) and April 2018 (S3B). OLCI is a 21 spectral channels instrument covering wavelengths between 400 nm and 1020 nm. Istomina et al. (2020) modified the algorithm developed by Zege et al. (2015) and refined by Istomina et al. (2020b) to apply it to OLCI observations to derive maps of the spectral albedo and of the melt-pond fraction per grid cell with the same spatial and temporal resolution and seasonal coverage as those derived from MERIS (see subsection 2.2.3). We use data of months May through August of years from 2017 through 2023 (Istomina et al., 2023, 2025), downloaded from https://data.seaice.uni-bremen.de/olci/, last access: 2023-10-27).

3 Processing Method

To create a new version of the data set, we used in general the same approach as Rösel et al (2012): a spectral unmixing procedure as originally proposed by Tschudi et al (2008), based on the recent MODIS Collection 6.1 MOD09GA product.

3.1 Preprocessing of the MODIS data

Since the MODIS data are given on a sinusoidal grid in separate tiles, we first of all reprojected the product to one netcdf file per day on a polar stereographic grid (EPSG 3413) with a spatial resolution of 500 meters. Regarding the parameters, we only considered the reflectance data of the bands 459-479 nm, 620-670 nm, 841-876 nm, and the two quality flag fields *sur_refl_state_500m* and *sur_refl_qc_500m*. In order to identify cloud free pixels, the bits 0, 1, 2, 8, 9, 10, 13 of the *sur_refl_state_500m* flag had to show the value zero; to get rid of land and coastal pixels we only considered bits 3-5 (land/water flag) showing values 111 (deep ocean), 110 (continental/moderate ocean), and 000 (shallow ocean). Regarding the *sur_refl_qc_500m* flag, the first two bits had to be zero (ideal quality).

3.2 Processing of the 500m data set

Based on this cloud and land free product on a polar stereographic grid, we calculated the fractions of three classes, i.e. melt ponds, sea ice free of melt ponds and open water between the sea-ice floes, by applying an optimization procedure as described in Rösel et al (2012).

The equation system (1) consists of the matrix **r,** containing the spectral reflectance values of the three surface types melt ponds (M), snow and ice (I), and open water (W) for the three different bands 1, 3, 4 of the MODIS data (see table 1), the

https://doi.org/10.5194/essd-2025-757
Preprint. Discussion started: 21 January 2026

Open Access Earth System Science Data Discussions

result vector **x** of the three surface type fractions, and the vector **R** containing the MODIS input data for the three bands. The last row of **r** and **R** makes sure that the sum of all fractions equals one.

$$\mathbf{r}\,\mathbf{x} = \mathbf{R}\,, \tag{1}$$

$$\text{with } \mathbf{r} = \begin{pmatrix} r_M(\lambda_1) & r_I(\lambda_1) & r_W(\lambda_1) \\ r_M(\lambda_3) & r_I(\lambda_3) & r_W(\lambda_3) \\ r_M(\lambda_4) & r_I(\lambda_4) & r_W(\lambda_4) \\ 1 & 1 & 1 \end{pmatrix}, \mathbf{x} = \begin{pmatrix} x_M \\ x_I \\ x_W \end{pmatrix}, \mathbf{R} = \begin{pmatrix} R(\lambda_1) \\ R(\lambda_3) \\ R(\lambda_4) \\ 1 \end{pmatrix},$$

Since the system is overdetermined – we have three variables in **x** but four equations – we could not calculate an analytic result. Therefore, we needed to approximate the solution by using an optimization approach. It consists in minimizing the following cost function:

$$f = (\mathbf{r}\,\mathbf{x} - \mathbf{R})^2\,, \tag{2}$$

Compared to Rösel et al. (2012), we applied two differences to their optimization approach:

1. We used different parameter values for our spectral bands 1, 3, and 4 compared to Rösel et al. (2012) because we wanted to establish a method, which is more comprehensible. Considering Fig. 2 of their publication, we estimated the mean value of all curves for each class and band (see table 1). As a result, we chose lower values for ice and open water than Rösel et al. (2012): our matrix **r** looks as follows:

$$\mathbf{r} = \begin{pmatrix} 0.22 & 0.86 & 0.05 \\ 0.16 & 0.85 & 0.05 \\ 0.07 & 0.72 & 0.05 \\ 1 & 1 & 1 \end{pmatrix}$$

2. We omitted the constraint term in our cost function (2), and applied an optimization function defining constraints so that the fraction values of the three surface type classes stay between 0 and 1. This procedure has the advantage that the fraction values could become exactly 0 or 1, respectively - or at least become closer to these values than this was the case in the approach of Rösel et al. (2012). The optimization function called TNC is implemented in Python's scipy.optimize package, and minimizes a function with variables subject to bounds, using gradient information in a truncated Newton-algorithm (https://docs.scipy.org/doc/scipy/reference/generated/scipy.optimize.fmin_tnc.html#scipy.optimize.fmin_tnc).

Table 1: Spectral reflectance values r_i of surface types used in the un-mixing algorithm.

https://doi.org/10.5194/essd-2025-757
Preprint. Discussion started: 21 January 2026

Open Access Earth System Science Data Discussions

MODIS band λ_i	Band width in nm	Meltpond r_M	Snow / Ice r_I	Open Water r_W
1	459-479	0.22	0.86	0.05
3	620-670	0.16	0.85	0.05
4	841-876	0.07	0.72	0.05

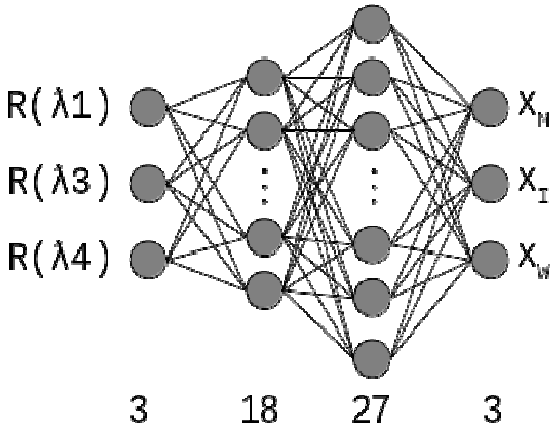

Figure 1: The architecture of the fully connected feed forward artificial neural network: 3 input neurons for the surface reflectance values of the three bands, 18 neurons in the first hidden layer, 27 in the second hidden layer, 3 output neurons for the three fractions (melt ponds, ice, water).

As in the approach of Rösel et al. (2012), the optimization process took too long to apply it to all days, so that we also implemented an artificial neural network (ANN) to speed up the classification for each pixel. We created two data sets, training and validation data, by calculating the optimization result for every 50th pixel of a subset of all dates: we considered May, June, July, and August of the years 2000, 2011, and 2020 to take into account most of the characteristic situations of reflectance distributions over the entire time period. Whether the resulting pair of reflectance and output vectors went into the training or validation data set was randomly chosen in the ratio 2 to 1, so that we got a set of 354754 training data and set of 183768 validation data. The architecture of the fully-connected feed-forward ANN (Fig 1), implemented by means of the Python module pytorch (https://pytorch.org/), is a bit different to the approach of Rösel et al. (2012) to reproduce the spatial variability in the optimization result data. The input layer has three neurons (for the three reflectance values), the first hidden layer has 18 neurons (compared to nine in Rösel et al. (2012)), the second hidden layer has 27 neurons. The output layer has three neurons for the three surface type classes melt ponds, ice and snow, and open water. As an activation function we applied the rectified linear unit function $ReLU(x)=(x)^+=max(0,x)$ to the output of each hidden layer neuron. The learning

https://doi.org/10.5194/essd-2025-757
Preprint. Discussion started: 21 January 2026

process where the weights were adjusted by backward propagation took place in 100 epochs with a learning rate of 0.15, the batch size for the shuffled training data was 100. These values achieved the highest accuracy of 99.85 % in a series of test runs without visible signs for overfitting since the evolution of the validation loss follows more or less the training loss curve (Fig 2).

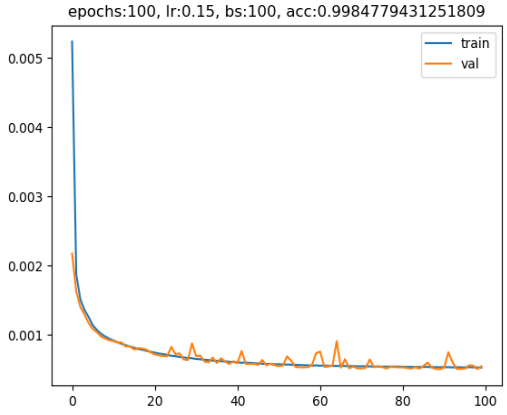

Figure 2: The evolution of the training (blue) and validation (orange) loss during the learning process over 100 epochs in the ANN. The learning rate was 0.15, the resulting accuracy of the ANN is 99.85 %.

We would like to clarify the fact that the optimization process was only used for creating the training and validation data, the actual processing of the three surface type fractions for every grid point was just based on the output of the ANN. The mean error that was introduced by using the ANN instead of the optimization process is 0.15 % according to the accuracy calculated in the test runs.

In the end, each day has a grid of 13286 by 13293 cells stored in a netCDF file containing the following parameters:

- **x_m**: grid-cell fraction of melt ponds
- **x_i**: grid-cell fraction of sea ice without melt ponds
- **x_w**: grid-cell fraction of open water between the sea ice
- **time** contains the current date
- projection coordinates **x** and **y** in meters.

The content of the complete netCDF header can be found in the appendix A. The metadata are stored following the CF conventions version 1.10. An additional file containing only latitude and longitude values for the 500 m product has been calculated and is provided together with the data set (Sadikni and Kern, 2025).

https://doi.org/10.5194/essd-2025-757
Preprint. Discussion started: 21 January 2026

3.3 Processing of the 12.5km data set

Based on the data set with 500 m grid resolution, we created a data set with 12.5 km grid resolution (Sadikni and Kern, 2025) by calculating the mean value of 25 x 25 adjacent grid cells. So, we get daily netCDF files containing a grid of 531 by 531 cells on the same polar stereographic projection including the following quantities:

- **mpf**: grid-cell fraction of melt ponds, computed if less than 90 percent of the 25 x 25 adjacent 500 m grid cells show the value NaN (same is required for **isf** and **owf**)
- **isf**: grid-cell fraction of sea ice without melt ponds, also called (net) ice surface fraction
- **owf**: grid-cell fraction of open water between the sea ice; **mpf** and **isf** only exhibit valid values if **owf** is less than 85 %, or – in other words – the 12.5 km grid needs to be covered with sea ice by at least 15 %.
- **mpf_stddev**, **isf_stddev** and **owf_stddev**: one standard deviation of the 25 x 25 input cells for the mean value calculation in the respective quantities **mpf**, **isf**, and **owf**.
- **mask_90percent_clearsky**: a mask indicating almost clear-sky conditions. It is set to 1 where less than 10 percent of the 25 x 25 cells exhibit the value NaN (i.e., 90 percent of the 500 m grid cells are flagged as clear-sky), and set to 0 otherwise. The mask can be easily multiplied with **mpf**, **isf**, or **owf** to obtain a clear-sky subset of these quantities.
- **number_of_valid_pixels**: Number of valid 500 m grid cells that are not NaN (regarding clear-sky conditions).
- projection coordinates **x** and **y** in meters.
- **lat** and **lon** values contain the corresponding latitude and longitude values.
- **time** contains the current date.

These and all other parameters can be found in the appendix B by means of a ncdump header of an example netCDF file. The metadata are stored according to the CF conventions version 1.10.

4 The melt-pond fraction data set

We show sample maps of three consecutive days (from 2009-07-02 through 2009-07-04) of our two data sets (Sadikni and Kern, 2025) in Figure 3: the first row depicts the 12.5 km data after the application of the clear-sky mask, the second one the 500 m data set. While the masked 12.5 km data set shows of course more gaps, the 500 m data set shows more noise. In general, one can see a coherent picture of the development of the open water, sea ice and melt-pond fraction within the three days shown.

https://doi.org/10.5194/essd-2025-757
Preprint. Discussion started: 21 January 2026

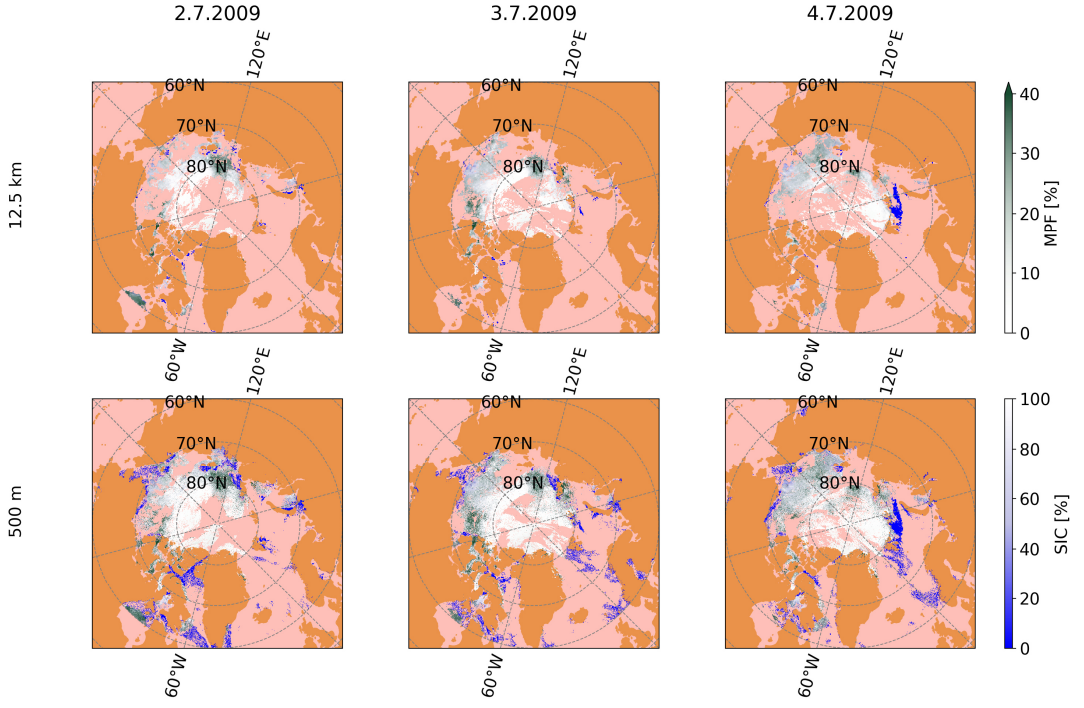

Figure 3: Three example maps of the 12.5 km (first row) and the 500 m data set (second row). There are two colour gradients: SIC from blue (0%) to white (100%), and the MPF from transparent (0%) to green-grey (>40%). Missing values are colour coded in salmon, land in orange (the darker colour of both).

We distributed the Arctic Ocean into five regions as shown in Fig. 4 a). For each of these regions, we computed the region-mean monthly mean values of the 12.5 km grid melt-pond fraction (**mpf**) and of the standard deviation of the melt-pond fraction resulting from the gridding process (**mpf_stddev**). We computed these mean values for the months June, July, and August of the years from 2000 through 2024 and show the resulting time series in Fig. 5.

https://doi.org/10.5194/essd-2025-757
Preprint. Discussion started: 21 January 2026

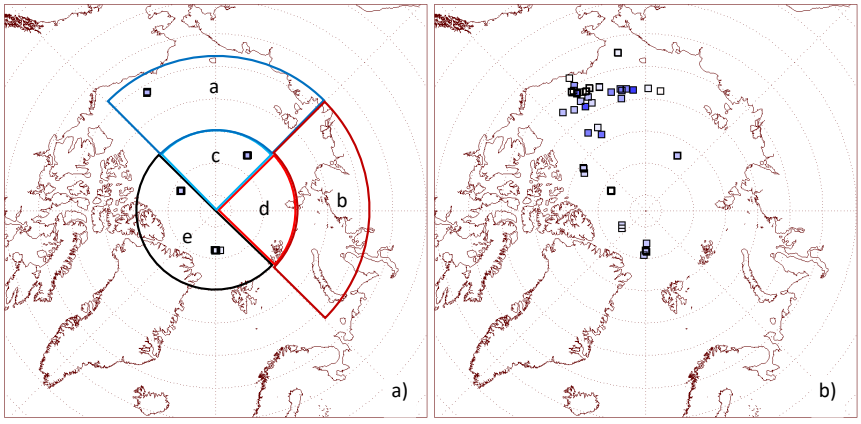

Figure 4: Locations of the satellite images used in the Fetterer et al. data set (a) and in the Webster et al. data set (b). In panel a) we mark the regions used in the time series shown in panels a) to e) in Figure 5.

We find mean melt-pond fractions of June to be, on average, larger in the southern regions (Fig. 5 a, b) than in the northern regions (Fig. 5 c-e). Values are around 10 % in region 45°E to 135°E (Fig. 5b) and between 10% and 15% in region 135°E to 225°E (Fig. 5 a) while in all other panels of Figure 5 the values of June are below 10 %. In most cases, we observe a June melt-pond fraction that is smaller than the one in July and/or August. Overall, we find the largest melt-pond fractions in the month of July in the southern regions: in 16 of the 25 years in region 135°E to 225°E (Fig. 5a) and in 13 of the 25 years in region 45°E to 135°E (Fig. 5b). In the regions north of 80°N, we find the largest melt-pond fractions in the month of August, in 13, 17, and 15 of the 25 years in region 135°E to 225°E (Fig. 5c), 45°E to 135°E (Fig. 5d) and 45°E to 135°W (Fig. 5e), respectively. We observe that the monthly mean melt-pond fraction increases from June to July to August for 13 to 15 years of the 25 years in the northern regions (Fig. 5 c-e), while in the southern regions we observe this temporal development only in eight (Fig. 5 a) or four years (Fig. 5 b). These findings are in agreement with the northward progression of surface melt.

The mean melt-pond fraction is influenced by the sea ice conditions and sea-ice type. Melt ponds on multiyear ice are usually smaller than those on first-year ice; therefore the melt-pond fraction is often smaller on multiyear ice than first-year ice (e.g. Perovich and Polashenski, 2012). Melt-pond fractions are also smaller on deformed ice than level ice. This helps us to interpret the time-series shown in Fig. 5. Particularly for the southern regions (Fig. 5 a, b) we find particularly small mean melt-pond fractions in August in several years, e.g. 2011, 2018, and 2024 (Fig. 5 b) or 2012, 2019, and 2024 (Fig. 5 a). For these years, the symbols denoting the mean melt-pond fraction are also quite small, signifying a very small number of valid data points contributing to the mean value. The number of valid data points can be heavily influenced by the number of grid cells discarded because of a too large or too persistent cloud coverage (see e.g. Fig. 5 d), June, years 2013 and 2021).

https://doi.org/10.5194/essd-2025-757
Preprint. Discussion started: 21 January 2026

Open Access Earth System Science Data Discussions

Nevertheless, in August, this number can be seen as an indicator for the amount of sea ice that is left in the respective region in the respective month (compare the values of N for June, July and August in Fig. 5 a, b)). If we observe an unusually small melt-pond fraction in August that is based on a relatively small number of grid cells, then it is likely that the sea ice carrying the melt ponds is either multiyear ice or heavily deformed and hence thick first-year ice, both being ice types where melt-pond fractions are known to be relatively small.

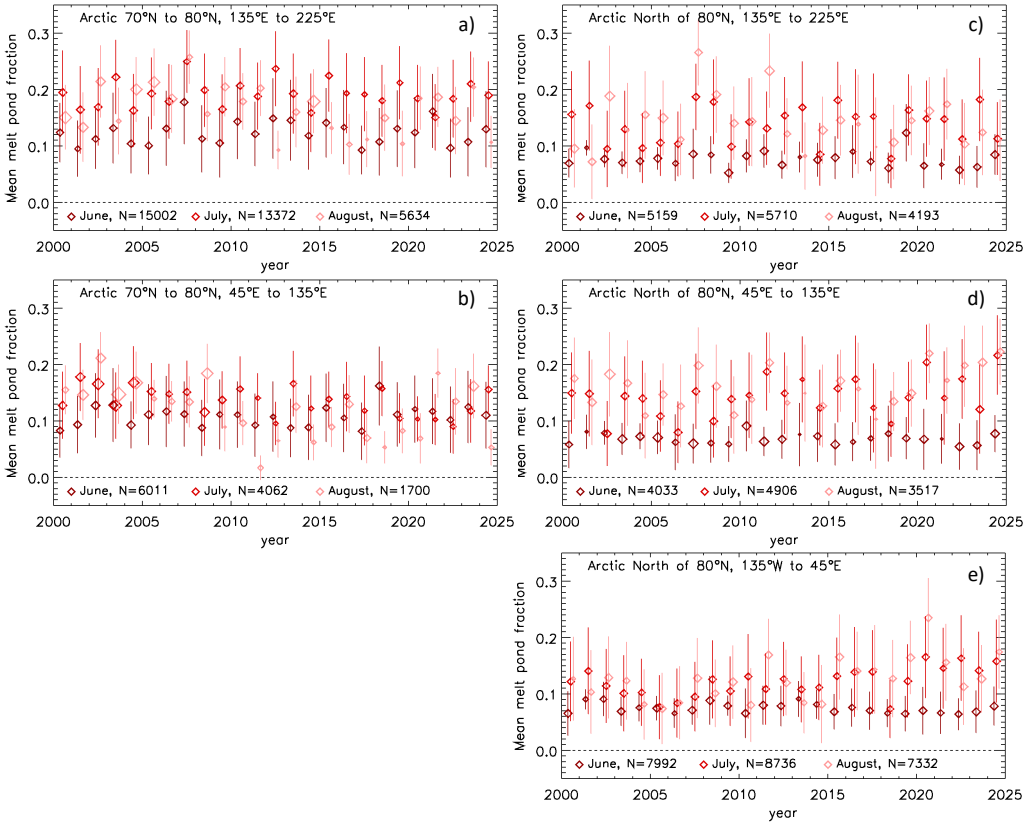

Figure 5: Time series of the monthly mean region average melt-pond fraction (symbols) and the monthly mean region average standard derivation (bars) derived from our data set for the entire time-period of years from 2000 through 2024. Data derived for the different months are shown in different colours. Symbol size scales with the number of valid grid cells used per month; the smaller the symbol the less valid data could be used. N is the total number of valid grid cells in the respective region for the respective month of the entire period. Regions are denoted at the top of every panel with the panel references a) to e) signifying regions shown in Fig. 4 a).

https://doi.org/10.5194/essd-2025-757
Preprint. Discussion started: 21 January 2026

Comparing the two adjacent regions for 135°E to 225°E (Fig. 5 a) and c)), reveals no obvious change in the melt-pond fractions in a specific month over the period of years shown. However, if we compare the two adjacent regions for 45°E to 135°E (Fig. 5 b) and d)), we find a tendency for a decrease in the August melt-pond fraction over the years in the southern region (panel b) while in the northern region (panel d) the August melt-pond fraction tends to increase. The same seems to apply to the July melt-pond fraction. Also, the region 45E° to 135°W seems to reveal an increase in both July and August melt-pond fractions over time. For instance, August melt-pond fractions stayed below 15 % before 2011 while during the last ten years we observed five incidences with August melt-pond fractions larger than 15 %.

Years 2007, 2012 and 2020 saw the three smallest Arctic sea-ice areas within the era of satellite remote sensing of the sea ice cover. In the year 2007, the minimum was strongly pre-conditioned by extensive melt in the Beaufort Sea, the Chukchi Sea, and the East Siberian Sea (e.g. Kay et al., 2008; Perovich et al., 2008; Nussbaumer and Pinker, 2012). This is reflected very well in our time series of MODIS melt-pond fraction. In 2007, region 135°E to 225°E reveals the maximum mean melt-pond fraction of the 25-year long record for June, July and August in its southern part (Fig. 5a) and for July and August in its northern part (Fig. 5c). The sea-ice area minima in 2012 and 2020 were different with respect to their development (e.g. Parkinson and Comiso, 2013). In 2012 we can see that the southern region 135°E to 225°E showed relatively large June (3rd largest) and July (2nd largest) mean melt-pond fractions (Fig. 5a), but none of the other regions reveals particularly large values. In 2020 we find maximum mean melt-pond fraction of the 25-year long record for July and August in region 45°E to 135°W and the 2nd largest mean melt-pond fraction for July and August in the northern region 45°E to 135°E.

5 Evaluation, Inter-comparison, and Discussion

5.1 Evaluation of the surface fractions at 500 m resolution

We illustrate a summary of the results of the comparison between MODIS surface fractions at 500 m grid resolution and respective surface fractions taken from the Webster et al. data set (see Subsection 2.2.1) in Figure 6. We refer to Fig. 9 a) to c) and Fig. 10 a) to c) for two examples of maps of the MODIS surface fractions at 500 m grid resolution superposed with Webster et al. surface fractions. On day 2007-06-10 (Fig. 9 a) to c)), MODIS under-estimates Webster et al. MPF values by about 10 % (median difference) while both ISF and OWF are over-estimated by about 5 %. For MPF and ISF, these differences belong to the extreme cases in our data set, i.e., they are located in the tails of the histograms shown in Fig. 6b), d). For OWF, the difference agrees with the modal difference (Fig. 6f). On day 2011-07-21 (Fig. 10 a) to c)), MODIS under-estimates Webster et al. MPF values by about 5 % while ISF and OWF are over-estimated by 1 % and 4 %, respectively.

https://doi.org/10.5194/essd-2025-757
Preprint. Discussion started: 21 January 2026

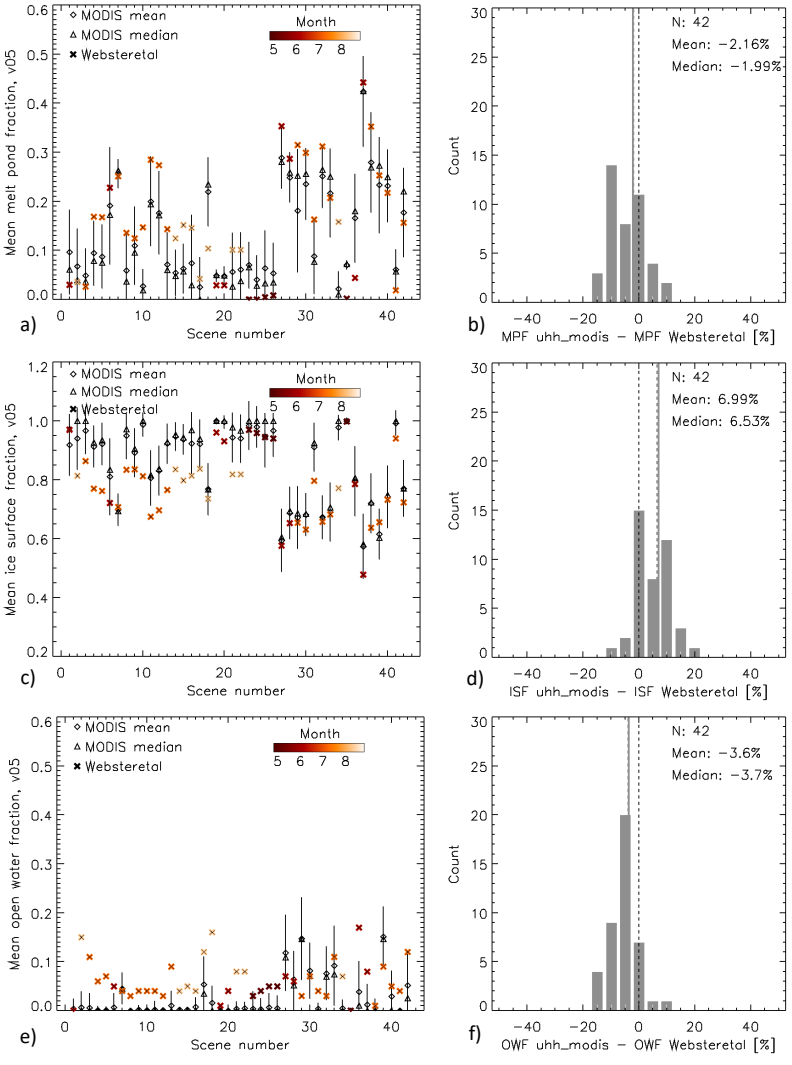

Figure 6: Comparison between mean and median MODIS results based on our 500 m grid resolution data set and the Webster et al. data set. On the left hand side we show results of each individual scene, on the right hand side we show histograms of the difference MODIS minus Webster et al.; from top to bottom: melt-pond fraction MPF (a, b), ice-surface fraction ISF (c, d), and open-water fraction OWF (e, f).

https://doi.org/10.5194/essd-2025-757
Preprint. Discussion started: 21 January 2026

Again putting these values into context with Fig. 6, reveals that for this day the differences for MPF and ISF are relatively common while the one for OWF is a rather uncommon value. Overall, we find a bi-modal distribution in the number of differences MODIS minus Webster et al. for MPF and ISF with primary peak modal values at -10 % and 0 %, respectively, and secondary peak modal values at 0 % and +10 %, respectively. On average, however, the MODIS product under-estimates Webster et al. MPF by about 2 % (Fig. 6 b) and overestimates the respective ISF by about 7 % (Fig. 6 d). Differences in the MPF range between -20 % and +20 %. Absolute differences and also the range of differences are smaller for OWF. Here we find an unimodal distribution of the differences, peaking at -5 % (Fig. 6 f); the mean is -3.7 %, i.e. OWF is slightly under-estimated in the 500 m MODIS product. The results for the Fetterer et al. data set are similar and shown together with the summary of the results for the Webster et al. data set in Table 2.

Table 2: Results of the comparison between our MODIS data sets at 500 m and at 12 500 m grid resolution and the data sets of Fetterer et al. and Webster et al. . MPF, ISF and OWF signify melt-pond, ice-surface (sea ice without melt ponds), and open-water fractions, respectively. N denotes the total number of valid data points. The results of the comparison with Webster et al. data includes the evaluation of the 12.5 km product for years from 2002 through 2011 which is the period of overlap with the MERIS MPF data set; note that the MERIS data set does not include values for the quantities ISF and OWF.

			MPF	ISF	OWF	N
Fetterer et al.	MODIS 2000-2001	Mean	-2.1 %	4.9 %	-1.9 %	14
		MAD	6.4 %	9.1 %	4.6 %	
Webster et al.	MODIS 2000-2014	Mean	-1.8 %	6.4 %	-3.4 %	42
		MAD	5.7 %	7.0 %	4.7 %	
	MODIS 2002-2011	Mean ; Median	-2.2 % ; -3.4 %	7.0 % ; 5.4 %	-3.8 % ; -3.7 %	35
	MERIS 2002-2011		7.8 % ; 9.0 %	-- ; --	-- ; --	

https://doi.org/10.5194/essd-2025-757
Preprint. Discussion started: 21 January 2026

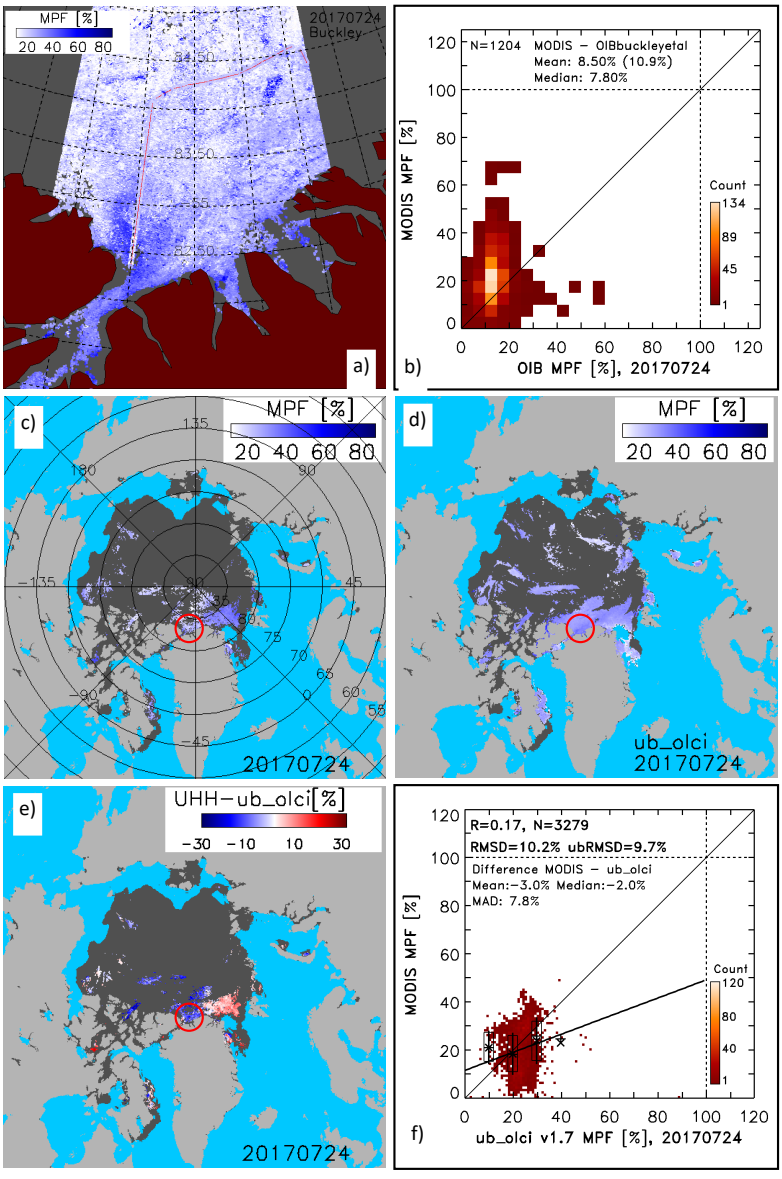

Figure 7: Comparison of our MODIS MPF data set at 500 m resolution with the MPF from OIB DMS imagery of day 2017-07-24 (top row) and of our MODIS MPF data set at 12.5 km resolution with the MPF from Sentinel-3 OLCI (middle and bottom row).

https://doi.org/10.5194/essd-2025-757
Preprint. Discussion started: 21 January 2026

MODIS MPF at 500 m superposed with Buckley et al. MPF in the Lincoln Sea (a); two-dimensional scatterplot (heat map) MODIS MPF versus OIB MPF (b); MODIS MPF map at 12.5 km (c), OLCI MPF map at 12.5 km (d); difference MODIS minus OLCI MPF (e); heat map MODIS MPF versus OLCI MPF (f). In panel (a), white patches denote open water, dark grey areas missing data. In panel (b), numbers denote the mean difference between MODIS MPF and Buckley et al. MPF and the standard deviation of the difference in parenthesis, followed by the median difference. In panels (c) through (e), dark grey denotes clouds; the red circle marks the location of OIB overflights. In panel (f), R, N, RMSD, ubRMSD, Mean, Median, and MAD denote the linear correlation coefficient, the number of valid data pairs, the Root Mean Squared Difference, the unbiased RMSD, the mean difference MODIS minus OLCI MPF, the median difference and the mean absolute difference, respectively. Symbols superposed onto the heat map denote statistical values computed from MODIS MPF for OLCI MPF bins [5 %-15 %[, [15 %-25 %[,[25 %-35 %[, and [35 %-45 %[with the X, the horizontal bar, the box size and the vertical bar denoting the mean, median, upper and lower quartile, and standard deviation of MODIS MPF.

Our MPF, ISF and OWF values at 500 m grid resolution compare reasonably well to values of these three quantities derived from OIB data (see Subsection 2.2.2). Of in total eight flights we found a sufficiently high number of overlapping grid cells for four, two flights each in the years 2016 and 2017. Figures 7a) and 8a) provide maps of the 500 m MODIS MPF data superposed with MPF values derived from the OIB data (Buckley et al., 2020). MODIS MPF values are mostly between 10 % and 20 % for both cases shown; only near the entry to Nares Strait (Fig. 7a) MODIS MPF values are considerably higher. Outside this area of high MODIS MPF, we find convincing visual agreement between MODIS and OIB MPF estimates. For day 2017-07-24 (Fig. 7 a,b) MODIS MPF overestimates OIB Buckley et al. MPF by 8.5 % (median 7.8 %) and underestimates OIB Wright et al. MPF by -1.7 % (median: -2.7 %). For day 2017-07-25 (Fig. 8 a,b) MODIS MPF overestimates OIB Buckley et al. MPF by 0.5 % (median: -2.8 %) and underestimates OIB Wright et al. MPF by -6.7 % (median: -8.4 %). We will discuss the results shown in panels c) to f) of Figures 7 and 8 in Subsection 5.2.

In summary (see Table 3), we find MODIS MPF to agree with OIB MPF by between -3 % (Wright et al.) and +4 % (Buckley et al., 2020). The standard deviation of the mean MPF difference is about 12 %. The agreement is better for ISF using the Buckley et al. data set (2.5 %) but worse using the Wright et al. data set (8.8 %); MODIS overestimates in both cases. For OWF we find that MODIS underestimates OIB OWF by -5 % to -6 %. The mean absolute difference (MAD) and mean differences are identical in magnitude for Buckley et al. MPF but not for Wright et al. MPF. For all four cases considered, MODIS MPF overestimates Buckley et al. OIB MPF systematically. Conversely, MAD and mean differences are identical in magnitude for ISF and OWF of the Wright et al. data set but not for the Buckley et al. data set. Hence, for these two quantities we find a systematic overestimation (underestimation) of the ISF (OWF) from the Wright et al. data set.

https://doi.org/10.5194/essd-2025-757
Preprint. Discussion started: 21 January 2026

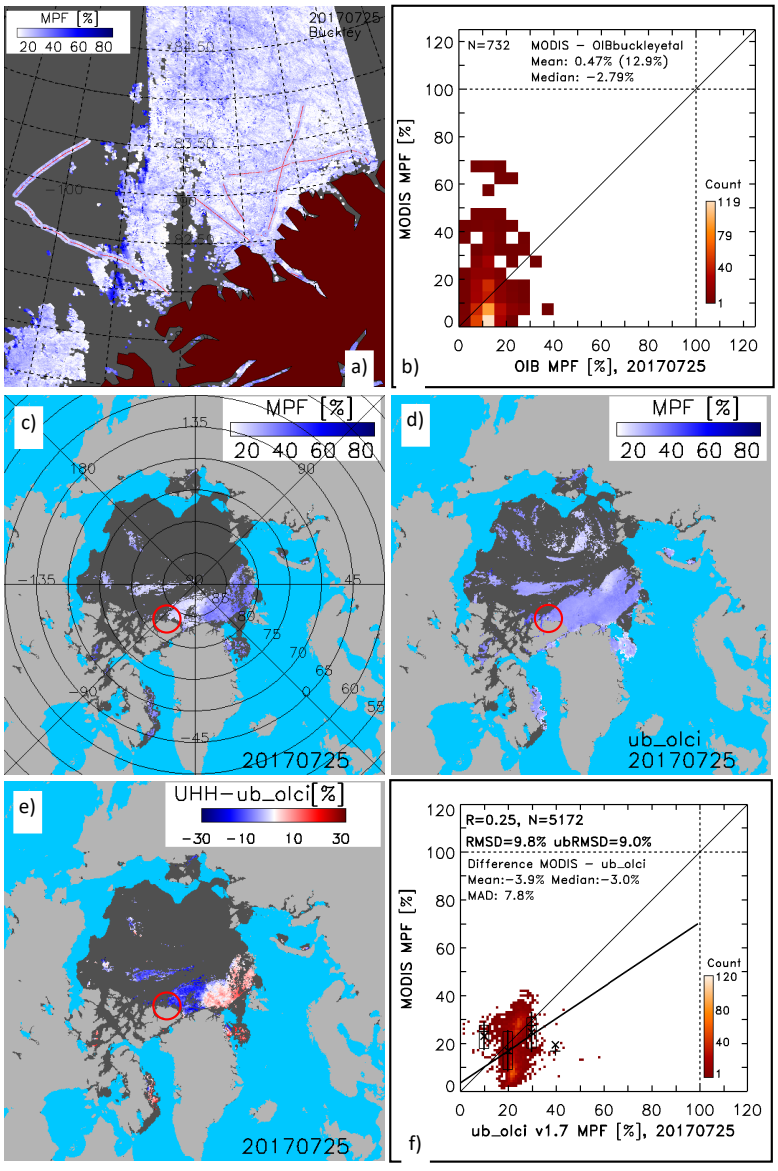

405 **Figure 8: As Figure 7 but using an OIB flight north of Ellesmere Island for day 2017-07-25.**

https://doi.org/10.5194/essd-2025-757
Preprint. Discussion started: 21 January 2026

Table 3: Mean and mean median difference and mean absolute difference (MAD) of our 500 m gridded MODIS data set minus the two OIB flight MPF estimates for two days each in 2016 and 2017 with > 50 valid overlapping grid cells. N denotes the total number of valid data points. MPF, ISF and OWF signify melt-pond, ice-surface, and open-water fractions, respectively. The mean MPF encountered was 16.0 % ± 8.1 %. The standard deviations of the differences are between 10 % and 15 %.

		MPF	ISF	OWF	N
Buckley et al.	Mean	4.2 %	2.5 %	-6.1 %	3116
	Median	3.3 %	3.4 %	-5.7 %	
	MAD	4.2 %	5.2 %	6.6 %	
Wright et al.	Mean	-2.7 %	8.8 %	-5.3 %	8113
	Median	-3.8 %	10.2 %	-3.6 %	
	MAD	3.3 %	8.8 %	5.3 %	

5.2 Inter-comparison of the 12.5 km surface type fraction data sets

Here we present the results of our inter-comparison of the 12.5 km surface type fraction data set with other, similar data sets based on MERIS or OLCI described in Subsections 2.2.3 and 2.2.4. First, we get back to Fig. 7 and Fig. 8. Panels c) and d) show the pan-Arctic melt-pond fraction of our data set and the OLCI data set, respectively, at 12.5 km grid resolution for day 2017-07-24 (Fig. 7) and day 2017-07-25 (Fig. 8). The OLCI data set MPF distribution is very homogeneous for both days (panel d) in Fig. 7 and Fig. 8), showing almost no spatial gradient. This is an observation we make for the MERIS MPF data set as well (see below). On both days, the OLCI data set shows considerably fewer grid cells discarded due to clouds than our data set. The main area of common overlap with clear-sky grid cells is located north of Greenland. The difference MODIS minus OLCI melt-pond fraction (panel e) is positive towards Fram Strait, e.g., roughly east of 45°W, and negative towards Beaufort Sea, e.g., roughly west of 45°W. Especially for day 2017-07-25 (Fig. 8e) we find a marked switch from around zero or slightly positive towards negative differences of the order of 15 % or more in magnitude. This observation is illustrated further by the 2-dimensional histograms (heat maps) shown in Fig. 7f) and Fig. 8f). Therein we can identify two clusters – again especially for day 2017-07-25 (Fig. 8f) – with one cluster located near to the 1-to-1 line of perfect agreement and one cluster located below that line. The resulting mean differences MODIS minus OLCI MPF are -3 % for 2017-07-24 and -4 % for 2017-07-25, i.e., MODIS MPF is smaller than OLCI MPF. The magnitude of this underestimation falls into the range of underestimation of the Wright et al. OIB MPF (see Section 5.1). The respective OIB overflights at both dates are

https://doi.org/10.5194/essd-2025-757
Preprint. Discussion started: 21 January 2026

located in regions where the difference MODIS minus OLCI MPF is particularly negative, i.e., where MODIS MPF seems to be offset from OLCI MPF by about 15 % (see Fig. 7e) and Fig. 8e)). Therefore, if we chose the bins with the highest count in the histograms shown in Fig. 7 b) and Fig. 8 b) we find for day 2017-07-24: MODIS: 20-25 %; OIB Buckley et al.: 10-15 %; OIB Wright et al. (not shown): 15-20 % and, applying the above-mentioned offset of 15 % between MODIS and OLCI, OLCI: 35-40 %. For day 2017-07-25, we find MODIS: 0-5 %; OIB Buckley et al.: 10-15 %; OIB Wright et al. (not shown): 15-20 % and OLCI: 15-20 %. Clearly, for 2017-07-24 the agreement to OIB MPF data sets is better for our MODIS MPF product while for 2017-07-25 the agreement is better for the OLCI MPF product.

We continue with showing two examples where we compare MODIS and MERIS MPF at 12.5 km grid resolution with the Webster et al. MPF for day 2007-06-10 (Fig. 9) and day 2011-07-21 (Fig. 10). For discussion of panels a) to c) we refer to Section 5.1. Similar to Fig. 7 and Fig. 8 we see that the MERIS MPF data set has considerably fewer grid cells marked as cloud-covered than the MODIS MPF data set for both days shown. We find a similar overestimation for our 12.5 km MODIS MPF data set than for the 500 m data set of ~8.0 %. MERIS MPF overestimates Webster et al. MPF by ~9 % (Fig. 9g) and h). While there is good consistency between MODIS and MERIS MPF values at that location (see red box in Fig. 9d), we find considerable differences in the MPF between these two data sets (Fig. 9d) to f) and i). These differences take values between -20 % and +20 %. Both MPF data sets generally agree in the location of high (southern Beaufort Sea and Chukchi Sea) and low (central Arctic Ocean) MPF values. However, MERIS MPF is near 0 % near the pole, while MODIS MPF values are considerably higher which is probably less realistic at this time of the seasonal cycle of MPF development. At the same time, MODIS MPF is near 0 % between the central Arctic and the southern Beaufort Sea while MERIS MPF values are considerably larger. This results in a quite heterogeneous distribution of MODIS minus MERIS MPF differences (Fig. 9f). The respective heat map (Fig. 9i) illustrates this heterogeneity quite well with two clusters where both data sets agree well but a relatively large cluster where both data sets disagree. In summary, MODIS MPF values are about 5 % smaller than MERIS MPF values.

For day 2011-07-21, the 12.5 km MODIS MPF data set underestimates Webster et al. MPF values by -3.5 %. MERIS MPF underestimates Webster et al. MPF values by -9.0 % - exactly opposite to day 2007-06-10. MERIS MPF maps (Fig. 10d), e) reveal a very homogeneous distribution. The MPF seems to be almost the same for the entire Arctic. In contrast, the MODIS MPF data set reveals values of < 10 % in the central Arctic and values towards 30 % in the Beaufort Sea, Chukchi Sea and Greenland Sea; there is a latitudinal gradient in the MPF. Consequently, the difference MODIS minus MERIS MPF (Fig. 10f) is quite negative in the central Arctic, and slightly positive towards the ice edges – which is where the respective Webster et al. data set scene is located (red box in Fig. 10d). The heat map (Fig. 10i) reflects very well our observation that MERIS MPF shows little variation, with values mostly confined to the range 20-25 % (see also the heat maps of the comparison to the OLCI MPF data in Fig. 7 and Fig. 8, panel d)), while MODIS MPF ranges from 0 % to 30 %. In summary, MODIS MPF values are about 8 % to 9 % smaller than MERIS MPF values in this case.

https://doi.org/10.5194/essd-2025-757
Preprint. Discussion started: 21 January 2026

Open Access Earth System Science Data Discussions

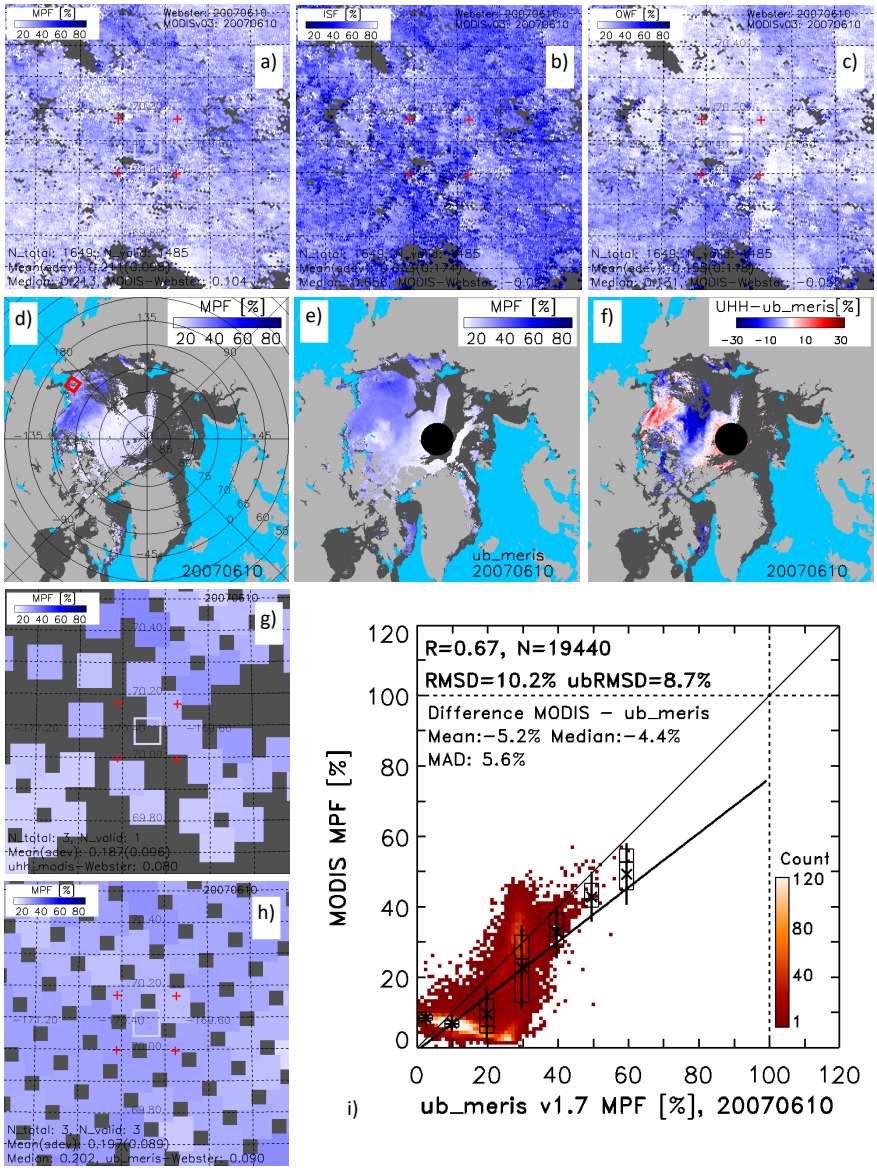

https://doi.org/10.5194/essd-2025-757
Preprint. Discussion started: 21 January 2026

Figure 9: Example of a particularly large difference between our MODIS MPF and Webster et al. MPF from day 2007-06-10. Top row: MODIS MPF (a), MODIS ISF (b) and MODIS OWF (c) superposed by a square coloured according to the respective parameter value in the Webster et al. data set. Each of these panels provide the number of MODIS parameter values falling into the area actually covered by the high-resolution optical image used in the Webster et al. data set – indicated by the red plus signs, the number of valid such points – aka clear sky, the mean MODIS parameter value and its standard deviation, the respective median value and the difference MODIS minus Webster et al. value of the respective parameter. Second row: MODIS MPF (d), MERIS MPF (e), and the difference MODIS minus MERIS MPF (f). Dark grey areas denote missing data due to clouds; black denotes the observational gap at the pole in the MERIS MPF data set. The red box in panel d) shows the approximate location of the area shown in panels a) to c). Panels g) and h) show a representation of the MODIS (g) and MERIS (h) gridded 12.5 km MPF data set superposed by the respective Webster et al. MPF as a coloured square (see also panel a). Dark grey areas denote clouds and gaps between the 12.5 km grid cells which are plotted such that their adjacent overlap is as small as possible while still covering the map almost completely. Values denoted at the bottom of panels g) and h) have notation similar to panel a). Panel i): 2-dimensional scatterplot of MODIS MPF versus MERIS MPF for the area of valid values shown in panel f). For the meaning of the black symbols and the values listed in panel i) we refer to Figure 7 f).

In combination, these two cases do not allow us to draw a conclusion about the correctness of the two MPF products compared. For day 2007-06-10, the differences to Webster et al. MPF are similar and the difference between the two gridded MPF products at that location is near zero. Hence, one could conclude that both gridded MPF data sets overestimate Webster et al. MPF by 5 to 10 %. To which other regions of the Arctic this result applies remains unclear. It is very likely, however, that in the central Arctic Ocean MERIS MPF is more realistic than MODIS MPF at this time of the year because MERIS MPF is near 0 % while MODIS MPF is around 5 %. For day 2011-07-21, the difference to Webster et al. MPF is smaller for MODIS than for MERIS, and MODIS MPF is larger than MERIS MPF. This is consistent and suggests that for that location MODIS MPF is more realistic than MERIS MPF. Our observation of a rather constant MERIS MPF value across the entire Arctic while MODIS MPF values exhibit a spatial gradient, suggests there are very likely more regions in the Arctic where for this case MODIS MPF is more realistic than the MERIS MPF. Figure 11 shows the histograms of the 35 cases where we have reasonable overlap between Webster et al. MPF images and the gridded MODIS and MERIS MPF data sets. Overall, MODIS MPF underestimates Webster et al. MPF by about 2 % on average (3-4 % in the median) while MERIS MPF overestimates Webster et al. MPF values by about 8 % on average (9 % in the median). This corresponds to a difference between the two data sets of the order of 10 %, which agrees well with the heat maps (Fig. 9i, 10i), and also supports the conclusion that, overall, the gridded MODIS MPF agrees better with the Webster et al. MPF data set.

https://doi.org/10.5194/essd-2025-757
Preprint. Discussion started: 21 January 2026

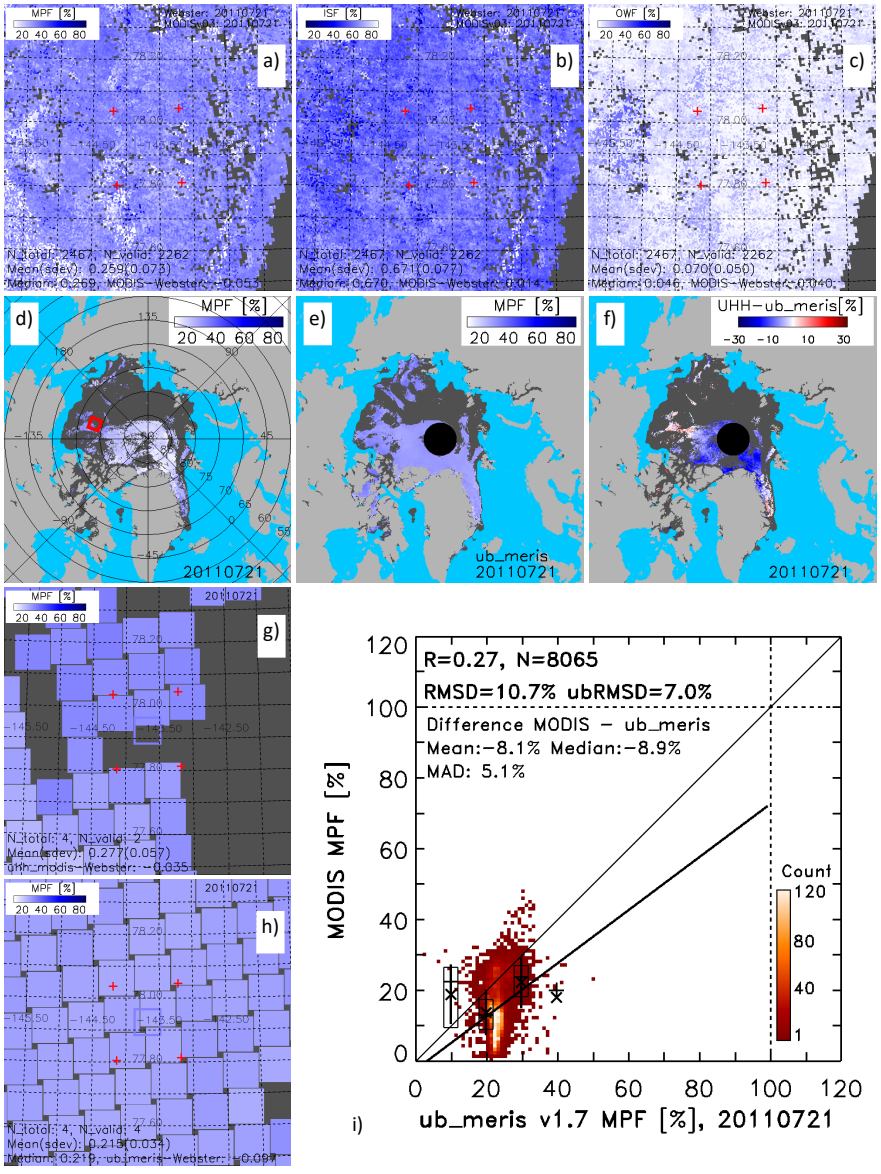

495 **Figure 10: As Figure 9 but for an example of a particularly low difference between MODIS MPF and Webster et al. MPF from day 2011-07-21.**

https://doi.org/10.5194/essd-2025-757
Preprint. Discussion started: 21 January 2026

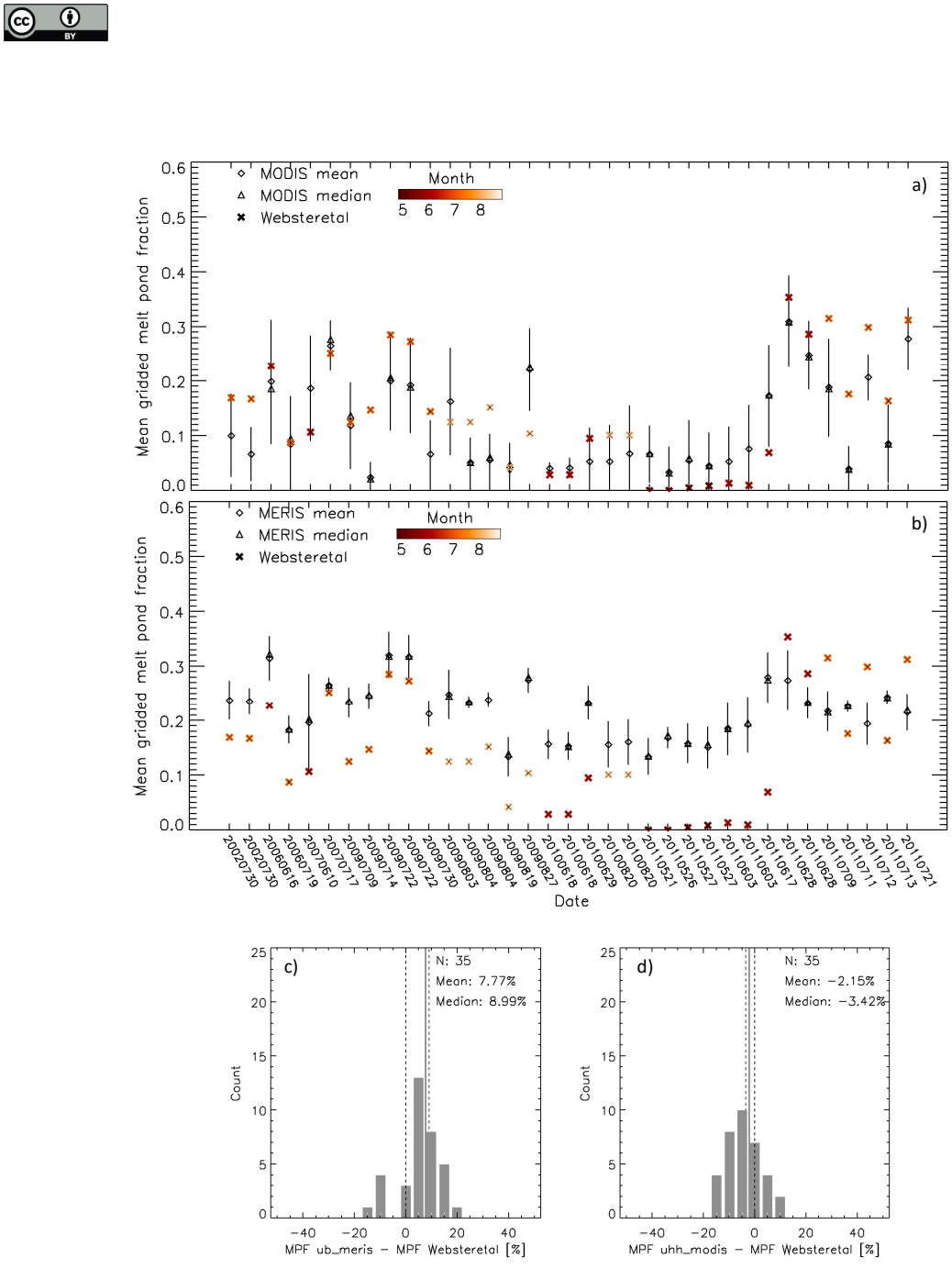

https://doi.org/10.5194/essd-2025-757
Preprint. Discussion started: 21 January 2026

Figure 11: Comparison between MODIS (a) or MERIS (b) MPF at 12.5 km grid resolution and Webster et al. MPF for the entire common overlap period of all three data sets. Only MODIS MPF 12.5 km grid cells with > 90 % clear-sky 500 m grid cells are used. The months of the Webster et al. MPF (crosses) are colour coded. Mean and median values are computed from all 12.5 km grid cells overlapping with the respective optical image used in Webster et al., the vertical bars denote one standard deviation from the gridding process used in the respective data set. Panels c) and d) show the distribution of the difference MERIS or MODIS MPF minus Webster et al. MPF for all cases shown in panels a) and b); mean and median values of the difference are given as number in the panel together with the number of the valid data pairs. The grey vertical lines denotes the mean difference.

Finally, in Figure 12 we illustrate the results of our comparison between the gridded MPF data sets for years from 2002 through 2011 for MERIS (panels on the left hand side) and for years from 2017 through 2023 for OLCI (panels on the right hand side). Overall, values of the median difference MODIS minus MERIS (or OLCI), unbiased RMSD, and linear correlation – all derived from a comparison like shown in the heat maps in Figures 9i) and 10i) – agree between MERIS and OLCI; values are similar. This is in line with our expectation because the algorithm used to derive MPF from MERIS and OLCI observations is the same. The median difference between MODIS MPF and the other two data sets is between 5 and 10 % in June and July and between 2 and 7 % in August. The agrees well with the finding shown in Fig. 11 for the comparison between MODIS and MERIS MPF data sets and the Webster et al. MPF data set; an overestimation of Webster et al. MPF by MERIS by 8 % coincides with an underestimation by MODIS by 2 %, hence a mean MPF difference between the two data sets of 10 %. We cannot show a figure similar to Figure 11 with results of a comparison between the 12.5 km MPF data sets (MODIS or OLCI) and OIB MPF estimates because we only have two cases in July 2017 with a sufficiently high number of clear-sky observations. Summing up our findings of the two cases shown in Figures 7 and 8 results in an over-estimation of Buckley et al OIB MPF by ~4 % by MODIS (at 500 m grid resolution) and in an under-estimation of Wright et al. OIB MPF by ~ -4 %. Overall, i.e., for all common clear-sky 12.5 km grid cells in the Arctic Ocean on those two days in 2017 OLCI MPF exceeds MODIS MPF by ~4 %. Applying this large-scale MPF offset to the OLCI MPF would result in an overestimation of the Buckley et al. OIB MPF by 8 % while OLCI MPF and Wright et al. OIB MPF would agree within < 1 %. The linear correlation between MODIS MPF on the one hand and each of the other data sets on the other hand is rather low, taking values around 0.4 in June and July, increasing to 0.5 to 0.6 in August. These low correlation values are consistent with our observation that both MERIS and OLCI MPF distributions tend to be rather homogeneous with little spatial variation or gradients while MODIS MPF distributions generally exhibit spatial gradients (see Figures 7 to 10). We note that values of the linear correlation in August tend to increase over the periods shown. However, we refrain from hypothesizing about the cause of this increase as this is beyond the scope of this publication.

https://doi.org/10.5194/essd-2025-757
Preprint. Discussion started: 21 January 2026

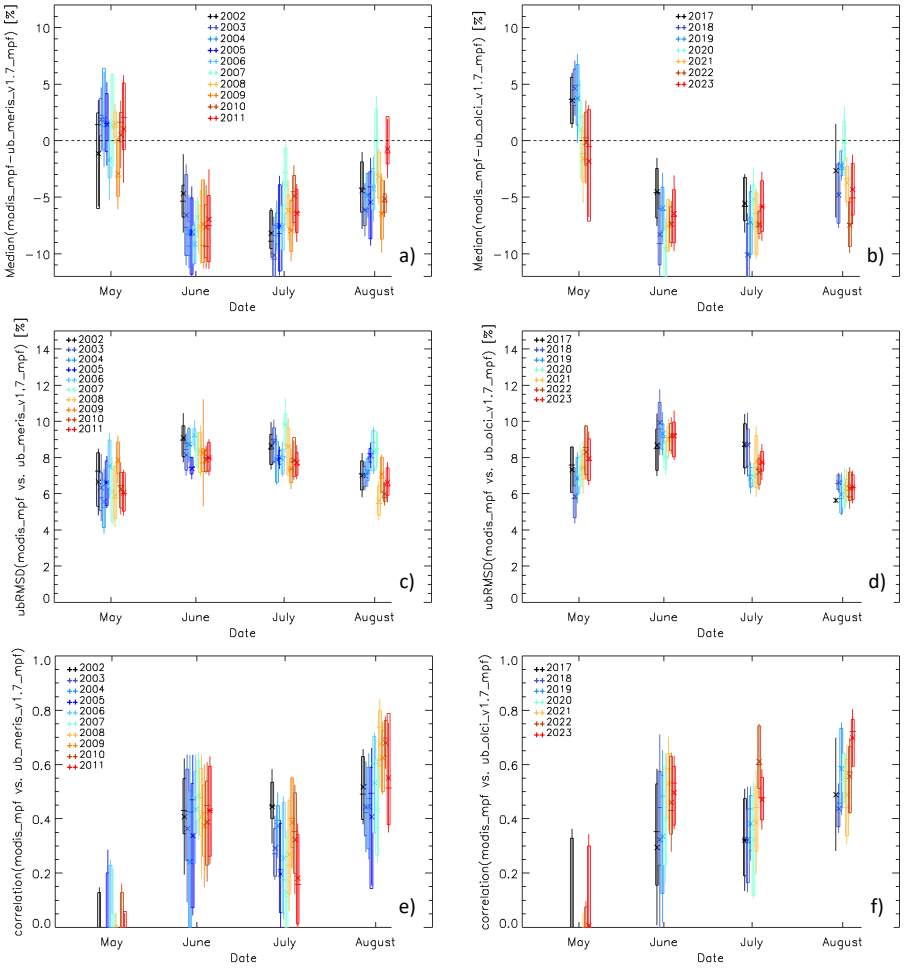

530 **Figure 12: Graphical illustration of the monthly mean values for May through August of the median difference MODIS MPF minus MERIS MPF (a) and MODIS MPF minus OLCI MPF (b), of the unbiased RMSD between MODIS and MERIS MPF (c) and MODIS and OLCI MPF (d), and of the respective linear correlation coefficient using MERIS MPF (e) and OLCI MPF (f) for each of the common years of overlap between the MPF data sets, i.e., from year 2002 through 2011 for MERIS and from year 2017 through 2023 for OLCI. Values are displaced slightly along the x-axis for enhanced visibility. Years are colour coded. Vertical**
535 **bars denote one standard deviation of the mean.**

https://doi.org/10.5194/essd-2025-757
Preprint. Discussion started: 21 January 2026

5.3 Discussion

One of the main results of our comparison between our 500 m resolution MODIS melt-pond fraction data set and the data sets from the independent high-resolution observations (space- and air-borne) is that we find quite variable differences between these data sets. Overall, we find an under-estimation of the MPF derived from high-resolution satellite observations by 2 % and a mis-estimation of the MPF derived from OIB digital camera imagery by 3 to 4 %. Individual differences commonly range between -10 % to -5 % to +5 to +10 %, in extreme cases |20 %|. While we find a tendency that large negative (positive) differences in MPF coincide with large positive (negative) differences in ISF (or ISF and OWF together) there is no rule behind it. We also observe, for instance, large negative (positive) differences in ISF that coincide with large positive (negative) difference of MPF and OWF together. Finding some rule or consistency in the observed differences would assist us in further improving the approach.

We are aware of the limitations inherent to our data set that come from both the choice of a spectral un-mixing approach and the usage of one set of frequencies to characterize the different surface types involved. The typical reflectance values we used for the three MODIS channels utilized in the processing to characterize the surface types: melt ponds, melt-pond free sea ice and open water (see Sect. 3.2 Table 1) obviously can only be a limited representation of the true spatiotemporal variation of spectral reflectance values. We have to consider two issues here. One is the large-scale (in space and time) variation of the surface properties across the Arctic. The other issue is the sub-grid scale variation of surface properties within a 500 m grid cell.

All surfaces involved, except the open water between the ice floes, exhibit a seasonal cycle in their spectral appearance. The spectral surface shortwave reflectance of snow changes as a function of its metamorphism related to the melting process with melting snow having a substantially lower reflectance than freshly fallen or cold snow. Likewise, snow free sea ice can exhibit a range of surface shortwave reflectance values depending on its melting stage. Also, inclusion of dust and sediments play a role. Finally, the spectral shortwave reflectance of the melt ponds themselves can change a lot of the course of the melting season. It depends on their depth and the type and stage of melting of the sea ice underneath. Recent overviews of the spectral shortwave reflectance of sea ice during summer are given, e.g., in Wright and Polashenski (2020) and Light et al. (2022). According to these overviews, for the wavelengths used in our MODIS-based approach, the spectral shortwave reflectance of melting sea ice ranges from 0.37 to 0.63, dirty ice exhibits reflectance values around 0.4 and that of melt ponds ranges from 0.07 to 0.56. With that melt-pond free sea ice and melt ponds can exhibit the same spectral shortwave reflectance. One such situation emerges, for instance, when young, shallow melt ponds (relatively high reflectance, e.g. 0.45) coexist with snow-free sea ice (relatively low reflectance, i.e. 0.65) – instead of ~0.2 versus ~0.8 (see Table 1). This situation might result in both, MPF under-estimation and ISF over-estimation or, the other way round. We find evidence for this situation in our results. Another possibility potentially emerges later in the season when melt ponds have matured, exhibiting reflectance values that are relatively close to those of the open water between the floes. This situation could result in MPF over-estimation and OWF under-estimation or the other way round. We find limited evidence for these cases, though. At the

https://doi.org/10.5194/essd-2025-757
Preprint. Discussion started: 21 January 2026

end, it is a question of how the samples that are used in the algorithm optimization and training process represent the different, seasonally varying surface conditions. We tried to take this variation into account be using training data for months May through August and years 2000, 2011, and 2020.

We are working with a spectral un-mixing approach, i.e. we are trying to derive the fractions of three different surface types within one 500 m grid cell from three reflectance values. While these three reflectance values are obtained at three different wavelengths (or frequencies), they cannot represent the true, sub-grid cell scale variation of surface reflectance values due to the different surface types that could be present in that 500 m grid cell. Usage of three different frequencies is not sufficient in this regard because different types of melt-pond free sea ice and different types of melt ponds can co-exist in one MODIS 500 m grid cell. The sea ice can be covered by fresh or melting snow, it can be snow free already, and it can be level or deformed, resulting in perhaps four or even five different surface shortwave reflectance values required to fully describe the true variation of the sea ice spectral signature between the melt ponds. Melt ponds can be shallow or deep, with or without a freeboard around them, and can be on different ice types (first-year ice vs. multiyear ice), resulting again in certainly more than one surface shortwave reflectance value required to fully describe the true variation of their spectral signature. The degree with which the set of reflectance values chosen in our approach represent this variety of surface conditions is unknown.

A natural solution to improve our setting would be to use more frequencies as was done, e.g., by Lee et al. (2020) who used four instead of three MODIS bands for melt pond detection and additional bands for cloud-shadow discrimination and filtering. However, according to Wright and Polashenski (2020) it is less the number of channels that is used in a spectral un-mixing approach but more the spatial and temporal variability of the surface spectral signature that limits the credibility of this approach when applied to the entire Arctic. They showed that local tuning of spectral shortwave reflectance values used in such an approach considerably reduces the difference to independent melt-pond fraction estimates from high-resolution WorldView imagery. They found a positive bias of 14 % in the melt-pond fraction between the MODIS MPF data set of Rösel et al. (2012, 2015) and their MPF estimates from WorldView imagery. The bias reduced to about 2 % when using an approach with locally tuned reflectance values – similar to the bias we obtained from the evaluation of our data set against independent high-resolution satellite or air-borne optical imagery (see Tables 2 to 4).

Wright and Polashenski (2020) could also demonstrate that such local tuning is not the solution when aiming for a pan-Arctic retrieval of the melt-pond fraction on sea ice. Another natural solution to the problem of the representation of the high spatiotemporal variation of surface types of sea ice during summer melt in satellite observations of the surface shortwave reflectance used for melt-pond fraction retrieval is to use satellite observations with a finer spatial resolution. While this has been done in the meantime with nearly pan-Arctic coverage based on Sentinel-2 MSI imagery (e.g., Wang et al., 2020; Niehaus et al., 2023), it does not solve the aim to provide an as long as possible time series of melt-pond fraction; Sentinel-2 MSI imagery has been available since June 2015. Our MODIS-based melt-pond fraction data set dates back to the year 2000.

We can see that the results of the inter-comparison with the two different OIB-based MPF data sets differ (Table 3). This applies in particular to the mean difference obtained for MPF (~4 % for Buckley et al. versus ~ -3 % for Wright et al.),

https://doi.org/10.5194/essd-2025-757
Preprint. Discussion started: 21 January 2026

but also for ISF (2.5 % for Buckley et al. versus ~9 % for Wright et al.). However, we attribute the differences in the results of our comparison to i) the different number and hence data points used in the inter-comparison (~3000 versus ~8000, see column "N" in Table 3) and ii) the different methodologies applied to estimate the surface fractions of melt ponds, pond-free sea ice, and open water. Buckley et al. used a pixel-based iterative threshold-based classification applied to Level 1 RGB imagery, first identifying sea ice, secondly identifying open water and at last separating open water between ice floes from open water on ice floes. Wright et al. applied a more complex multi-step approach (see Wright et al., 2020) to Level 0 raw reflectivity values of the digital images to classify four different surface types in one go. In an attempt to quantify how much the two methods differ when compared to our 500 m grid resolution MODIS data set, we derived a subset of the results shown in Table 3, using only those OIB images that coincide in both data sets and provide valid data. We show the results of this exercise in Table 4.

Table 4: Mean and mean median difference and mean absolute difference (MAD) of our 500 m gridded MODIS data set minus the two OIB flight MPF estimates for one day in 2016 and two days in 2017 with > 50 valid *identical* (see text for more information) overlapping grid cells. This is a subset of the results shown in Table 3. See Table 3 for meaning of acronyms. The mean absolute difference between Buckley et al. and Wright et al. daily mean differences MODIS minus OIB is 3.6 %, 4.3 %, and 3.4 % for MPF, ISF, and OWF, respectively.

		MPF	ISF	OWF	N
Buckley et al.	Mean	4.1 %	2.5 %	-6.1 %	1917
	Median	3.5 %	3.2 %	-5.7 %	
	MAD	5.2 %	2.6 %	6.1 %	
Wright et al.	Mean	0.6 %	6.8 %	-6.8 %	
	Median	-0.4 %	6.8 %	-5.4 %	
	MAD	2.6 %	8.4 %	6.8 %	

Based on about 1900 valid data we find similar mean values of the difference MODIS minus OIB for OWF; both methods exhibit a larger OWF for OIB than for MODIS (by around 6 %). In contrast, Buckley et al. OIB ISF is closer to MODIS ISF than Wright et al. OIB ISF (2.5 % versus 6.8 %, difference: 4.3 %) and Wright et al. OIB MPF is closer to MODIS MPF than Buckley et al. OIB MPF (0.6 % versus 4.1 %, difference: 3.5 %). Based on the results shown in Table 4 we propose to apply an average uncertainty of ± 1 % for the OIB OWF estimates and of ± 4 % for the respective ISF and MPF estimates. With that the mean difference Buckley et al. OIB MPF minus MODIS MPF is ~4 % ± 4 %, the mean difference Wright et al. OIB MPF minus MODIS MPF is ~ -3 % ± 4 %, and the mean differences for ISF are 2.5 % ± 4 % and ~9 % ± 4 % Buckley et al. and Wright et al., respectively.

https://doi.org/10.5194/essd-2025-757
Preprint. Discussion started: 21 January 2026

We find maps of the 12.5 km OLCI and MERIS MPF data sets to be surprisingly homogeneous with little spatial variability – especially during July. In contrast, maps of the 12.5 km MODIS MPF data set often show considerable but quite realistic gradients in the MPF distribution. We showed two cases, both from July (2017-07-24 and 2017-07-25), of a comparison between MODIS and OLCI MPF for which we have OIB-based estimates of the MPF (Fig. 7 and 8). The result of this comparison is inconclusive. In one of the cases (2017-07-25), we find a mean difference for MODIS minus OIB MPF (at 500 m grid resolution) that is close to zero, while in the other case (2017-07-24) we find a mean difference of ~8 %, i.e. MODIS MPF > OIB MPF. We cannot do the same inter-comparison for the OLCI MPF data set at 500 m grid resolution. But we can compare the 12.5 km data sets. In both cases, OLCI MPF is, on average, about 3 to 4 % larger than MODIS MPF (see panel f) in Fig. 7 and 8). This is, however, the average difference and panel e) of Fig. 7 and 8 clearly reveals a bi-polar distribution of the difference between our MODIS MPF data set and the OLCI MPF data set. For both cases, differences are negative (MODIS MPF < OLCI MPF) west of about 45°W and positive (MODIS MPF > OLCI MPF) east of 45°W. This means also, that in both cases the differences obtained with the OIB MPF data set fall into the region where MODIS MPF < OLCI MPF by 10 % or even more (see panel e) of Figures 7 and 8). For 2017-07-25, the case with a close to zero difference between MODIS and OIB MPF, this means that OLCI MPF is overestimating OIB MPF by 10 % or more. For 2017-07-24, the case where MODIS MPF overestimates OIB MPF by about 8 %, this means that OLCI MPF is overestimating OIB MPF even more, likely by close to 20 %. While these considerations cannot replace a 1-to-1 validation of OLCI MPF data at 500 m grid resolution as we did with our MODIS MPF data set, these provide context for the comparison between MODIS and OLCI MPF. They suggest that the agreement we have obtained between MODIS MPF and OIB MPF is very likely better than the agreement we would have obtained between OLCI MPF and OIB MPF.

We find quite some variability in the differences between MERIS MPF and Webster et al. MPF on the one hand and MODIS MPF and Webster et al. MPF on the other hand. We tend to conclude that both products have their difficulties; MODIS MPF is slightly too high (~5 %) in the central Arctic early in the melt season, i.e. first half of June. MERIS MPF is too homogeneous. Overall, the difference between Webster et al. and MERIS is considerably larger (MERIS overestimates by 8%) than the one for MODIS (MODIS underestimates by 2 %). With that, the MODIS MPF data set appears to be more realistic overall when compared to the Webster et al. MPF data set.

MODIS, MERIS and OLCI MPF data sets are influenced by clouds. Filtering of clouds is done differently between the MODIS MPF data set (see Section 3) and both the MERIS and OLCI data sets (Istomina et al., 2025). As one of the consequences we find that the 12.5 km MODIS data set offers considerably less grid cells with valid data than the other two 12.5 km MPF data sets. We note, however, that the maps of the 12.5 km MODIS MPF data set we show in this publication are solely based on the version of the data set where at least 90 % of the 500 m pixels used to compute the 12.5 km MPF value are valid – i.e., are for instance classified as confident clear sky. This is different from the procedure used in Istomina et al. (2025). They use a swath-based cloud mask and include pixels, which are cloud-free during at least one overpass into the daily product. Before the gridding, an edge of two pixels on the cloud-free areas in the swath data is removed. For their 12.5 km data set, at least 50 cloud-free pixels (pixel size is 300 m for OLCI) are required to form a valid gridded estimate of

https://doi.org/10.5194/essd-2025-757
Preprint. Discussion started: 21 January 2026

the MPF (Istomina et al., 2025). As there fit about 1700 300 m x 300 m pixels into one 12.5 km x 12.5 km grid cell, this minimum of 50 cloud-free pixels translates into about 3%. Hence, gridded OLCI (and MERIS) MPF values are available when 3 % of the 12.5 km x 12.5 km grid cell are identified as cloud-free. This explains the above-mentioned observation that the maps of our 12.5 km MODIS data set show substantially fewer valid values. In contrast to the OLCI and MERIS MPF data set, we require 90 % of the 500 m pixels to be cloud-free for the maps shown. Such a filtering is possible with our MODIS MPF data set because we include the number of valid 500 m pixels used for the 12.5 km grid resolution data set. We could not find a data layer in the netCDF files of the OLCI and MERIS MPF data sets of Istomina et al. (2025) that would have allowed us to filter the data in a similar manner. In a recent publication, Buckley et al. (2024) used MODIS imagery to detect the ice floe size distribution in the Beaufort Sea; they state that about 58 % of the images from years 2000 through 2023 are cloud covered, hindering further processing. Actually, their Figure 5a) even suggests a cloud fraction between 65 % and 70 % for the time period relevant for our melt-pond fraction data set. This underlines that cloud coverage is likely to seriously limit MPF retrieval using MODIS but also all other satellite sensors such as MERIS or OLCI.

6 Data availability

Our daily melt pond and net ice surface fraction data set is available here: https://doi.org/10.25592/uhhfdm.18069. The MODIS Terra collection 6.1 product MOD09A1 of the surface spectral reflectance are available as sinusoidal grid tiles from https://lpdaac.usgs.gov/products/mod09gav061/. Our data for evaluation and inter-comparison are from: Fetterer et al., 2008, http://nsidc.org/data/G02159/versions/1; Webster et al., 2015, http://psc.apl.uw.edu/melt-pond-data/; Polashenski et al., 2020, https://doi.org/10.5067/1LI57H56EB7G; Buckley et al., 2020, ftp://ftp.star.nesdis.noaa.gov/pub/socd/lsa/SeaIceProducts/Airborne/IceBridge/SummerMelt/; Istomina et al., 2023, https://data.seaice.uni-bremen.de/meris/mecosi/; Istomina et al., 2023, 2025, https://data.seaice.uni-bremen.de/olci/.

7 Code availability

The complete code for processing this data set can be found here: https://gitlab.rrz.uni-hamburg.de/BAO4478/modis_meltpondfraction.

8 Conclusions

In this paper, we present a novel 25-years long data set of the gridded daily melt-pond fraction (MPF) on sea ice in the Arctic. We offer MPF data for the months June to August for the years 2000 through 2024 at 500 m and at 12.5 km grid resolution on the NSIDC polarstereographic grid. Alongside the MPF, we also provide the open-water fraction (OWF), i.e., the grid-cell area fraction of open water between the sea-ice floes, and the fraction of sea ice without melt ponds, called ice-

https://doi.org/10.5194/essd-2025-757
Preprint. Discussion started: 21 January 2026

surface fraction (ISF). The gridded 12.5 km data set also includes the standard deviation resulting from the process of averaging 500 m grid cells onto 12.5 km grid resolution, and a mask that enables to filter out cases with more than 10 % cloud coverage. We describe the processing steps that led to this novel data set. We present and discuss the content of the data set, and describe, illustrate and discuss the validation and inter-comparison of our data set against independent air-borne and space-borne estimates of the MPF and the other two quantities. Our MODIS MPF agrees within -3 % to +4 % with independent estimates of the MPF from very-high resolution optical satellite imagery and Operation Ice Bridge Digital Camera System imagery. Our MODIS OWF values are too small by 2 % to 6 % and our MODIS ISF values tend to be too large by 2 % to 9 % compared to these independent data. Our novel 12.5 km MODIS data set under-estimates the MPF from very-high resolution optical satellite imagery by about 2 % in the mean (median: 3 %) while the MERIS product over-estimates these independent MPF estimates by about 8 % (median: 9 %). We could show that the novel MODIS MPF data set exhibits more realistic pan-Arctic MPF gradients than other medium-resolution satellite-based MPF data sets. Our MODIS MPF data set cannot compete with the quality of similar data sets based on more recent high-resolution satellite observations, e.g. Sentinel-2 MSI, because the used spectral un-mixing approach has limitations in representing the true variability of the different stages of sea ice melt that are often co-existing in a 500 m MODIS grid cell. However, its (current) length of 25 years, the daily temporal resolution, and an overall mean bias in MPF below 4% when compared to very-high resolution satellite image and air-borne optical imagery makes it a valuable addition to the currently existing suite of melt-pond fraction data sets.

Author contributions

RS modified the original algorithm and carried out all processing steps that led to the final product. SK obtained and pre-processed all validation data and carried out the validation. RS and SK jointly wrote the manuscript.

Competing interests

The authors declare that they don't have any competing interests or potential conflicts of interest

Acknowledgements

This manuscript is a contribution to the Cluster of Excellence: CLICCS – Climate, Climatic Change, and Society

https://doi.org/10.5194/essd-2025-757
Preprint. Discussion started: 21 January 2026

References

Aparício, S., S. Driscoll, and D. Flocco (2025) Observational data of Arctic Sea Ice Melt Ponds: a Systematic Review of Acquisition and Processing Approaches, EGUsphere, https://doi.org/10.5194/egusphere-2025-4480.

Barber, D. D., and J. Yackel (2000). The physical, radiative and microwave scattering characteristics of melt ponds on Arctic landfast sea ice. Int. J. Rem. Sens., 20(10), 2069-2090.

Buckley, E. M., Farrell, S. L., Duncan, K., Connor, L. N., Kuhn, J. M., and Dominguez, R. T. (2020). Classification of sea ice summer melt features in high-resolution IceBridge imagery. Journal of Geophysical Research: Oceans, 125(5), e2019JC015738. https://doi.org/10.1029/2019JC015738

Fetterer, F., and N. Untersteiner (1998) Observations of melt ponds on Arctic sea ice. J. Geophys. Res.-Oceans, 103(C11), 24821-24835.

Fetterer, F., S. Wilds, and J. Sloan. 2008. Arctic sea ice melt pond statistics and maps, 1999-2001. Boulder, Colorado USA: National Snow and Ice Data Center. http://dx.doi.org/10.7265/N5PK0D32 (last access: 2023-09-05).

Fors, A. S., Divine, D. V., Doulgeris, A. P., Renner, A. H. H., and Gerland, S. (2017) Signature of Arctic first-year ice melt pond fraction in X-band SAR imagery. The Cryosphere, 11(2), 755-771, https://doi.org/10.5194/tc-11-755-2017.

Howell, S. E. L., Scharien, R. K., Landy, J., and Brady, M. (2020) Spring melt pond fraction in the Canadian Arctic Archipelago predicted from RADARSAT-2. The Cryosphere, 14(12), 4675-4686, https://doi.org/10.5194/tc-14-4675-2020.

Istomina, L., Niehaus, H., and G. Spreen (2025) Updated Arctic melt pond fraction dataset and trends 2002–2023 using ENVISAT and Sentinel-3 remote sensing data, The Cryosphere, 19, 83-105, https://doi.org/10.5194/tc-19-83-2025.

Istomina, L., Marks, H., Huntemann, M., Heygster, G., and Spreen, G. (2020a) Improved cloud detection over sea ice and snow during Arctic summer using MERIS data, Atmos. Meas. Tech., 13, 6459–6472, doi.org/10.5194/amt-13-6459-2020.

Istomina, L., Heygster, G., Huntemann, M., Schwarz, P., Birnbaum, G., Scharien, R., Polashenski, C., Perovich, D., Zege, E., Malinka, A., Prikhach, A., and Katsev, I. (2015a) Melt pond fraction and spectral sea ice albedo retrieval from MERIS data – Part 1: Validation against in situ, aerial, and ship cruise data, The Cryosphere, 9, 1551–1566, https://doi.org/10.5194/tc-9-1551-2015.

Istomina, L., Heygster, G., Huntemann, M., Schwarz, P., Birnbaum, G., Scharien, R., Polashenski, C., Perovich, D., Zege,

https://doi.org/10.5194/essd-2025-757
Preprint. Discussion started: 21 January 2026

E., Malinka, A., Prikhach, A., and Katsev, I. (2015b) Melt pond fraction and spectral sea ice albedo retrieval from MERIS data – Part 2: Case studies and trends of sea ice albedo and melt ponds in the Arctic for years 2002–2011, The Cryosphere, 9, 1567–1578, https://doi.org/10.5194/tc-9-1567-2015

Istomina, L.: Reprocessed MECOSI cloud screened MPD MPFs, Institute for Environmental Physics, University of Bremen, Bremen [data set], https://seaice.uni-bremen.de/data/meris/mecosi/ (last access: 2023-08-20), 2023a.

Istomina, L.: The OLCI MPD MPF dataset, Institute for Environmental Physics, University of Bremen, Bremen [data set], https://seaice.uni-bremen.de/data/olci/ (last access: 2023-08-30), 2023b.

Kay, J. E., T. L'Ecuyer, A. Gettelman, G. Stephens, and C. O'Dell (2008) The contribution of cloud and radiation anomalies to the 2007 Arctic sea ice extent minimum, Geophys. Res. Lett., 35, L08503, https://doi.org/10.1029/2008GL033451.

Kramer, M., and R. Kiko (2011) Brackish meltponds on Arctic sea ice - a new habitat for marine metazoans. Polar Biology, 34, 603-608. https://doi.org/10.1007/s00300-010-0911-z

Landy, J., J. Ehn, M. Shields, and D. Barber (2014), Surface and melt pond evolution on landfast first-year sea ice in the Canadian Arctic Archipelago, J. Geophys. Res. Oceans, 119, 3054–3075, https://doi.org/10.1002/2013JC009617 .

Lee, S., Stroeve, J., Tsamados, M., and Khan, A. L. (2020) Machine learning approaches to retrieve pan-Arctic melt ponds from visible satellite imagery, Remote Sens. Environ., 247, 0034–4257, https://doi.org/10.1016/j.rse.2020.111919.

Light, B., Smith, M. M., Perovich, D. K., Webster, M. A., Holland, M. M., Linhardt, F., Raphael, I. A., Clemens-Sewall, D., Macfarlane, A. R., Anhaus, P. and Bailey, D. A. (2022) Arctic sea ice albedo: Spectral composition, spatial heterogeneity, and temporal evolution observed during the MOSAiC drift, Elementa: Science of the Anthropocene, 10(1), 000103, https://doi.org/10.1525/elementa.2021.000103.

Lu, P., Leppäranta, M., Cheng, B., and Li, Z. (2016) Influence of melt-pond depth and ice thickness on Arctic sea-ice albedo and light transmittance. Cold Regions Sci. Technol., 124, 1-10, https://doi.org/10.1016/j.coldregions.2015.12.010 .

Mäkynen, M., Kern, S., Rösel, A., and Pedersen, L. T. (2014) On the estimation of melt pond fraction on the Arctic sea ice with Envisat WSM images. IEEE Trans. Geosci. Rem. Sens., 52(11), 7366-7379, https://doi.org/10.1109/TGRS.2014.2311476 .

https://doi.org/10.5194/essd-2025-757
Preprint. Discussion started: 21 January 2026

Markus, T., Cavalieri, D. J., Tschudi, M. A., and Ivanoff, A. (2003) Comparison of aerial video and Landsat 7 data over ponded sea ice. Rem. Sens. Environ., 86(4), 458-469, https://doi.org/10.1016/S0034-4257(03)00124-X .

MODIS/Terra Surface Reflectance 8-Day L3 Global 500 m SIN Grid V061 – MOD09A1, Vermote, E., MODIS/Terra Surface Reflectance 8-Day L3 Global 500m SIN Grid V061. 2021, distributed by NASA EOSDIS Land Processes DAAC, doi:10.5067/MODIS/MOD09A1.061 , Accessed YYYY-MM-DD.

Niehaus, H. Spreen, G., Birnbaum, G., Istomina, L., Jäkel, E., Linhardt, F., Neckel, N., Fuchs, N., Nicolaus, M., Sperzel, T., Tao, R., Webster, M., and Wright, N. (2023) Sea Ice Melt Pond Fraction Derived From Sentinel-2 Data: Along the MOSAiC Drift and Arctic-Wide, Geophys. Res. Lett., 50, e2022GL102102, https://doi.org/10.1029/2022GL102102.

Niehaus, H., Istomina, L., Nicolaus, M., Tao, R., Malinka, A., Zege, E., and Spreen, G. (2024) Melt pond fractions on Arctic summer sea ice retrieved from Sentinel-3 satellite data with a constrained physical forward model, The Cryosphere, 18, 933–956, https://doi.org/10.5194/tc-18-933-2024.

Nussbaumer, E. A., and R. T. Pinker (2012) The role of shortwave radiation in the 2007 Arctic sea ice anomaly, Geophys. Res. Lett., 39, L15808, https://doi.org/10.1029/2012GL052415.

Palmer, M. A., B. T. Saenz, and K. R. Arrigo (2014) Impacts of sea ice retreat, thinning, and melt-pond proliferation on the summer phytoplankton bloom in the Chukchi Sea, Arctic Ocean. Deep Sea Res.-II, 105, 85-104. https://doi.org/10.1016/j.dsr2.2014.03.016.

Parkinson, C. L., and J. C. Comiso (2013) On the 2012 record low Arctic sea ice cover: Combined impact of preconditioning and an August storm, Geophys. Res. Lett., 40, 1356–1361, https://doi.org/10.1002/grl.50349.

Perovich, D. K., W. B. Tucker III, and K. A. Ligett (2002a) Aerial observations of the evolution of ice surface conditions during summer, J. Geophys. Res., 107(C10), 8048, https://doi.org/10.1029/2000JC000449.

Perovich, D. K., T. C. Grenfell, B. Light, and P. V. Hobbs (2002b) Seasonal evolution of the albedo of multiyear Arctic sea ice, J. Geophys. Res., 107(C10), 8044, https://doi.org/10.1029/2000JC000438.

Perovich, D. K., J. A. Richter-Menge, K. F. Jones, and B. Light (2008), Sunlight, water, and ice: Extreme Arctic sea ice melt during the summer of 2007, Geophys. Res. Lett., 35, L11501, https://doi.org/10.1029/2008GL034007

https://doi.org/10.5194/essd-2025-757
Preprint. Discussion started: 21 January 2026

Perovich, D. K., and C. Polashenski (2012), Albedo evolution of seasonal Arctic sea ice, Geophys. Res. Lett., 39, L08501, https://doi.org/10.1029/2012GL051432.

Perovich, D. K. (2018) Sunlight, clouds, sea ice, albedo, and the radiative budget: the umbrella versus the blanket. The Cryosphere, 12(6), 2159-2165, https://doi.org/10.5194/tc-12-2159-2018

Petrich, C., H. Eicken, C. M. Polashenski, M. Sturm, J. P. Harbeck, D. K. Perovich, and D. C. Finnegan (2012) Snow dunes: A controlling factor of melt pond distribution on Arctic sea ice, J. Geophys. Res., 117, C09029, https://doi.org/10.1029/2012JC008192.

Polashenski, C., D. Perovich, and Z. Courville (2012) The mechanisms of sea ice melt pond formation and evolution, J. Geophys. Res., 117, C01001, https://doi.org/10.1029/2011JC007231.

Rösel, A., Kaleschke, L. and Birnbaum, G. (2012). Melt ponds on Arctic sea ice determined from MODIS satellite data using an artificial neural network. The Cryosphere, 6(2), 431–446, https://doi.org/10.5194/tc-6-431-2012 .

Rösel, A., Kaleschke, L. and Kern, S. (2013). Gridded Melt Pond Cover Fraction on Arctic Sea Ice derived from TERRA-MODIS 8-day composite Reflectance Data. World Data Center for Climate (WDCC) at DKRZ. https://doi.org/10.1594/WDCC/MODIS__Arctic__MPF

Rösel, A., Kaleschke, L., and Kern, S. (2015). Gridded Melt Pond Cover Fraction on Arctic Sea Ice derived from TERRA-MODIS 8-day composite Reflectance Data bias corrected Version 02, https://www.cen.uni-hamburg.de/en/icdc/data/cryosphere/arctic-meltponds.html . World Data Center for Climate (WDCC) at DKRZ. https://doi.org/10.1594/WDCC/MODIS__Arctic__MPF_V02

Sadikni, R., and Kern, S. (2025). Daily melt-pond fraction on Arctic sea ice from TERRA MODIS visible imagery Version 2025_fv0.01) [Data set]. https://doi.org/10.25592/uhhfdm.18069[last access: 2026-01-05].

Sankelo, P., Haapala, J., Heiler, I., and Rinne E. (2010). Melt pond formation and temporal evolution at the drifting station Tara during summer 2007. Polar Res., 29(3), 311-321, https://doi.org/10.1111/j.1751-8369.2010.00161.x

Scharien, R. K., J. J. Yackel, D. G. Barber, M. Asplin, M. Gupta, and D. Isleifson (2012) Geophysical controls on C band polarimetric backscatter from melt pond covered Arctic first-year sea ice: Assessment using high-resolution scatterometry, J. Geophys. Res., 117, C00G18, https://doi.org/10.1029/2011JC007353.

https://doi.org/10.5194/essd-2025-757
Preprint. Discussion started: 21 January 2026

Tanaka, Y., Tateyama, K., Kameda, T., and Hutchings, J. K. (2016) Estimation of melt ponds fraction over high concentration Arctic sea ice using AMSR-E passive microwave data, J. Geophys. Res.-Oceans, 121, 7056–7072, https://doi.org/10.1002/2016JC011876.

Tilling, R., Kurtz, N. T., Bagnardi, M., Petty, A. A., and Kwok, R. (2020) Detection of melt ponds on Arctic summer sea ice from ICESat-2. Geophys. Res. Lett., 47, e2020GL090644. https://doi.org/10.1029/2020GL090644.

Tschudi, M. A., Maslanik, J. A., and Perovich, D. K. (2008). Derivation of melt pond coverage on Arctic sea ice using MODIS observations. Remote Sensing of Environment, 112(5), 2605–2614, https://doi.org/10.1016/j.rse.2007.12.009 .

Wang, M., Su, J., Landy, J., Leppäranta, M., and Guan, L. (2020). A new algorithm for sea ice melt pond fraction estimation from high-resolution optical satellite imagery. Journal of Geophysical Research: Oceans, 125, e2019JC015716. https://doi.org/10.1029/2019JC015716

Webster, M. A., I. G. Rigor, D. K. Perovich, J. A. Richter-Menge, C. M. Polashenski, and B. Light (2015), Seasonal evolution of melt ponds on Arctic sea ice, J. Geophys. Res. Oceans, 120, https://doi.org/10.1002/2015JC011030 .

Wright, N. C., Polashenski, C. M., McMichael, S. T., and Beyer, R. A. (2020) Observations of sea ice melt from Operation IceBridge imagery. The Cryosphere, 14(10), 3523-3536, https://doi.org/10.5194/tc-14-3523-2020

Wright, N. C., and Polashenski, C. M. (2020). How machine learning and high-resolution imagery can improve melt pond retrieval from MODIS over current spectral unmixing techniques. J. Geophys. Res., 125, e2019JC015569, https://doi.org/10.1029/2019JC015569

Wright, N. C., and Polashenski, C. M. (2018). Open-source algorithm for detecting sea ice surface features in high-resolution optical imagery. The Cryosphere, 12(4), 1307–1329, https://doi.org/10.5194/tc-12-1307-2018

Yackel, J. J., and Barber, D. G. (2000) Melt ponds on sea ice in the Canadian Archipelago 2. On the use of RADARSAT-1 synthetic aperture radar for geophysical inversion. J. Geophys. Res.-Oceans, 105(C9), 22061-22070,

Zege, E., Malinka, A., Katsev, I., Prikhach, A., Heygster, G., Istomina, L., Birnbaum, G., and Schwarz, P. (2015) Algorithm to retrieve the melt pond fraction and the spectral albedo of Arctic summer ice from satellite optical data, Remote Sens. Environ., 163, 153–164, https://doi.org/10.1016/j.rse.2015.03.012.

Appendix

A. ncdump output of a 500m netCDF

https://doi.org/10.5194/essd-2025-757
Preprint. Discussion started: 21 January 2026


```
netcdf MODIS__MeltPondFraction__UHAM-ICDC__v04__500m__20140611 {
dimensions:
        x = 13286 ;
        y = 13293 ;
        time = 1 ;
variables:
        double x(x) ;
                x:standard_name = "projection_x_coordinate" ;
                x:long_name = "x coordinate of projection" ;
                x:units = "m" ;
        double y(y) ;
                y:standard_name = "projection_y_coordinate" ;
                y:long_name = "y coordinate of projection" ;
                y:units = "m" ;
        float x_m(time, y, x) ;
                x_m:_FillValue = -99.f ;
                x_m:units = "1" ;
                x_m:grid_mapping = "polarstereographic_projection" ;
                x_m:long_name = "grid_cell_fraction of melt ponds" ;
        float x_i(time, y, x) ;
                x_i:_FillValue = -99.f ;
                x_i:units = "1" ;
                x_i:grid_mapping = "polarstereographic_projection" ;
                x_i:long_name = "grid_cell_fraction of sea ice without melt ponds" ;
        float x_w(time, y, x) ;
                x_w:_FillValue = -99.f ;
                x_w:units = "1" ;
                x_w:grid_mapping = "polarstereographic_projection" ;
                x_w:long_name = "grid_cell_fraction of open water" ;
        int64 time(time) ;
                time:units = "seconds since 2000-01-01 00:00:00" ;
                time:calendar = "standard" ;
                time:standard_name = "time" ;
        int64 polarstereographic_projection ;
                polarstereographic_projection:grid_mapping_name = "polar_stereographic" ;
                polarstereographic_projection:latitude_of_projection_origin = 70. ;
                polarstereographic_projection:longitude_of_central_meridian = -45. ;
                polarstereographic_projection:scale_factor_at_projection_origin = 1. ;

// global attributes:
                :Conventions = "CF-1.10" ;
                :institution = "University of Hamburg" ;
                :creator = "remon.sadikni@uni-hamburg.de" ;
```

https://doi.org/10.5194/essd-2025-757
Preprint. Discussion started: 21 January 2026

:title = "melt ponds on arctic sea ice (500m)" ;
string :description = "This data set was created by means of a spectral unmixing procedure as proposed by Tschudi et al (2008) and Rösel et al (2011) based on the MODIS Collection 6.1 MOD09GA data. The results are daily fractions of melt ponds, sea ice and open water per 500m grid cell." ;
string :references = "Roesel, A., Kaleschke, L., and Birnbaum, G. (2012). Melt ponds on Arctic sea ice determined from MODIS satellite data using an artificial neural network. The Cryosphere, 6(2), 431–446. https://doi.org/10.5194/tc-6-431-2012, Tschudi, M. A., Maslanik, J. A., and Perovich, D. K. (2008). Derivation of melt pond coverage on Arctic sea ice using MODIS observations. Remote Sensing of Environment, 112(5), 2605–2614. https://doi.org/10.1016/j.rse.2007.12.009" ;
:source = "Vermote, E., Wolfe, R. (2021). MODIS/Terra Surface Reflectance Daily L2G Global 1km and 500m SIN Grid V061 MOD09GA.061. NASA EOSDIS Land Processes Distributed Active Archive Center. Accessed 2024-08-21 from https://doi.org/10.5067/MODIS/MOD09GA.061" ;
:NCO = "netCDF Operators version 5.1.8 (Homepage = http://nco.sf.net, Code = http://github.com/nco/nco, Citation = 10.1016/j.envsoft.2008.03.004)" ;
:history = "Mon Nov 10 18:00:56 2025: ncatted -a long_name,x_w,o,c,grid_cell_fraction of open water DAILY/2014/MODIS__MeltPondFraction__UHAM-ICDC__v04__500m__20140611.nc\nMon Nov 10 18:00:56 2025: ncatted -a long_name,x_i,o,c,grid_cell_fraction of sea ice without melt ponds DAILY/2014/MODIS__MeltPondFraction__UHAM-ICDC__v04__500m__20140611.nc\nMon Nov 10 18:00:56 2025: ncatted -a long_name,x_m,o,c,grid_cell_fraction of melt ponds DAILY/2014/MODIS__MeltPondFraction__UHAM-ICDC__v04__500m__20140611.nc" ;
}

B. ncdump output of a 12.5km netCDF

netcdf MODIS__MeltPondFraction__UHAM-ICDC__v03__12500m__20140831 {
dimensions:
time = 1 ;
y = 531 ;
x = 531 ;
variables:
float mpf(time, y, x) ;
mpf:_FillValue = -999.f ;
mpf:units = "1" ;
mpf:grid_mapping = "polarstereographic_projection" ;
mpf:cell_methods = "area: mean" ;
mpf:long_name = "grid_cell_fraction of melt ponds" ;
short number_of_valid_pixels(time, y, x) ;
number_of_valid_pixels:long_name = "number of clear sky grid cells" ;
number_of_valid_pixels:units = "1" ;
number_of_valid_pixels:grid_mapping = "polarstereographic_projection" ;

https://doi.org/10.5194/essd-2025-757
Preprint. Discussion started: 21 January 2026


```
                number_of_valid_pixels:comment = "number of clear sky grid cells of the original
500m product" ;
        byte mask_90percent_clearsky(time, y, x) ;
                mask_90percent_clearsky:flag_values = "0b,1b" ;
                mask_90percent_clearsky:flag_meanings = "clouds clearsky" ;
                mask_90percent_clearsky:long_name = "clear sky mask" ;
                mask_90percent_clearsky:units = "1" ;
                mask_90percent_clearsky:grid_mapping = "polarstereographic_projection" ;
                mask_90percent_clearsky:comment = "1: clear sky, number_of_valid_pixels greater
than 562.5, which is 90 percent of 625 cells, 0: not clear sky" ;
        float mpf_stddev(time, y, x) ;
                mpf_stddev:_FillValue = -999.f ;
                mpf_stddev:units = "1" ;
                mpf_stddev:grid_mapping = "polarstereographic_projection" ;
                mpf_stddev:long_name = "grid_cell_fraction of melt ponds standard_deviation" ;
        float owf(time, y, x) ;
                owf:_FillValue = -999.f ;
                owf:units = "1" ;
                owf:grid_mapping = "polarstereographic_projection" ;
                owf:cell_methods = "area: mean" ;
                owf:long_name = "grid_cell_fraction of open water" ;
        float owf_stddev(time, y, x) ;
                owf_stddev:_FillValue = -999.f ;
                owf_stddev:units = "1" ;
                owf_stddev:grid_mapping = "polarstereographic_projection" ;
                owf_stddev:long_name = "grid_cell_fraction of open water standard_deviation" ;
        float isf(time, y, x) ;
                isf:_FillValue = -999.f ;
                isf:units = "1" ;
                isf:grid_mapping = "polarstereographic_projection" ;
                isf:cell_methods = "area: mean" ;
                isf:long_name = "grid_cell_fraction of sea ice without melt ponds" ;
        float isf_stddev(time, y, x) ;
                isf_stddev:_FillValue = -999.f ;
                isf_stddev:units = "1" ;
                isf_stddev:grid_mapping = "polarstereographic_projection" ;
                isf_stddev:long_name = "grid_cell_fraction of sea ice without melt ponds
standard_deviation" ;
        float lat(y, x) ;
                lat:units = "degrees_north" ;
                lat:standard_name = "latitude" ;
        float lon(y, x) ;
                lon:units = "degrees_east" ;
```

https://doi.org/10.5194/essd-2025-757
Preprint. Discussion started: 21 January 2026


```
                lon:standard_name = "longitude" ;
        double x(x) ;
                x:standard_name = "projection_x_coordinate" ;
                x:long_name = "x coordinate of projection" ;
                x:units = "m" ;
        double y(y) ;
                y:standard_name = "projection_y_coordinate" ;
                y:long_name = "y coordinate of projection" ;
                y:units = "m" ;
        int64 time(time) ;
                time:units = "seconds since 2000-01-01 00:00:00" ;
                time:calendar = "standard" ;
                time:standard_name = "time" ;
        int64 polarstereographic_projection ;
                polarstereographic_projection:grid_mapping_name = "polar_stereographic" ;
                polarstereographic_projection:latitude_of_projection_origin = 70. ;
                polarstereographic_projection:longitude_of_central_meridian = -45. ;
                polarstereographic_projection:scale_factor_at_projection_origin = 1. ;

// global attributes:
                :Conventions = "CF-1.10" ;
                :institution = "University of Hamburg" ;
                :creator = "remon.sadikni@uni-hamburg.de" ;
                :title = "melt ponds on arctic sea ice (12.5km)" ;
                :description = "This data set contains daily fractions of melt ponds, sea ice and
open water per 12.5km grid cell obtained by averaging the 500m product." ;
                string :references = "Roesel, A., Kaleschke, L., and Birnbaum, G. (2012). Melt
ponds on Arctic sea ice determined from MODIS satellite data using an artificial neural network.
The Cryosphere, 6(2), 431–446. https://doi.org/10.5194/tc-6-431-2012, Tschudi, M. A., Maslanik, J.
A., and Perovich, D. K. (2008). Derivation of melt pond coverage on Arctic sea ice using MODIS
observations. Remote Sensing of Environment, 112(5), 2605–2614.
https://doi.org/10.1016/j.rse.2007.12.009" ;
                :source = "500m melt pond fraction product" ;
                :NCO = "netCDF Operators version 5.1.8 (Homepage = http://nco.sf.net, Code =
http://github.com/nco/nco, Citation = 10.1016/j.envsoft.2008.03.004)" ;
                :history = "Mon Nov 10 16:28:51 2025: ncatted -a
long_name,owf_stddev,o,c,grid_cell_fraction of open water standard_deviation
DAILY/2014/MODIS__MeltPondFraction__UHAM-ICDC__v03__12500m__20140831.nc\nMon Nov 10 16:28:51
2025: ncatted -a long_name,owf,o,c,grid_cell_fraction of open water
DAILY/2014/MODIS__MeltPondFraction__UHAM-ICDC__v03__12500m__20140831.nc\nMon Nov 10 16:28:51
2025: ncatted -a long_name,isf_stddev,o,c,grid_cell_fraction of sea ice without melt ponds
standard_deviation DAILY/2014/MODIS__MeltPondFraction__UHAM-ICDC__v03__12500m__20140831.nc\nMon
Nov 10 16:28:50 2025: ncatted -a long_name,isf,o,c,grid_cell_fraction of sea ice without melt
```

https://doi.org/10.5194/essd-2025-757
Preprint. Discussion started: 21 January 2026

Open Access Earth System Science Data Discussions

ponds DAILY/2014/MODIS__MeltPondFraction__UHAM-ICDC__v03__12500m__20140831.nc\nMon Nov 10 16:28:50 2025: ncatted -a long_name,mpf_stddev,o,c,grid_cell_fraction of melt ponds standard_deviation DAILY/2014/MODIS__MeltPondFraction__UHAM-ICDC__v03__12500m__20140831.nc\nMon Nov 10 16:28:50 2025: ncatted -a long_name,mpf,o,c,grid_cell_fraction of melt ponds DAILY/2014/MODIS__MeltPondFraction__UHAM-ICDC__v03__12500m__20140831.nc" ;
}